



# An Insight-HXMT Dedicated 33 day Observation of SGR J1935+2154. II. Burst Spectral Catalog

Ce Cai<sup>1,2</sup>, Shao-Lin Xiong<sup>1</sup>, Lin Lin<sup>3</sup>, Cheng-Kui Li<sup>1</sup>, Shuang-Nan Zhang<sup>1,2</sup>, Wang-Chen Xue<sup>1,2</sup>, You-Li Tuo<sup>1</sup>, Xiao-Bo Li<sup>1</sup>, Ming-Yu Ge<sup>1</sup>, Hai-Sheng Zhao<sup>1</sup>, Li-Ming Song<sup>1,2</sup>, Fang-Jun Lu<sup>1,2</sup>, Shu Zhang<sup>1</sup>, Qing-Xin Li<sup>3</sup>, Shuo Xiao<sup>1,2</sup>, Zhi-Wei Guo<sup>1,4</sup>, Sheng-Lun Xie<sup>1,5</sup>, Yan-Qiu Zhang<sup>1,2</sup>, Qi-Bin Yi<sup>1,6</sup>, Yi Zhao<sup>1,3</sup>, Zhen Zhang<sup>1</sup>, Jia-Cong Liu<sup>1,2</sup>, Chao Zheng<sup>1,2</sup>, and Ping Wang<sup>1</sup>

<sup>1</sup> Key Laboratory of Particle Astrophysics, Institute of High Energy Physics, Chinese Academy of Sciences, 19B Yuquan Road, Beijing 100049, People's Republic of China; [xiongsl@ihep.ac.cn](mailto:xiongsl@ihep.ac.cn), [lick@ihep.ac.cn](mailto:lick@ihep.ac.cn)

<sup>2</sup> University of Chinese Academy of Sciences, Chinese Academy of Sciences, Beijing 100049, People's Republic of China

<sup>3</sup> Department of Astronomy, Beijing Normal University, Beijing 100088, People's Republic of China; [llin@bnu.edu.cn](mailto:llin@bnu.edu.cn)

<sup>4</sup> College of Physics Sciences Technology, Hebei University, No. 180 Wusi Dong Road, Lian Chi District, Baoding City, Hebei Province 071002, People's Republic of China

<sup>5</sup> School of Physical Science and Technology, Central China Normal University, Wuhan 430097, People's Republic of China

<sup>6</sup> School of Physics and Optoelectronics, Xiangtan University, Xiangtan 411105, Hunan, People's Republic of China

Received 2022 March 18; revised 2022 April 14; accepted 2022 April 14; published 2022 June 17

## Abstract

Since 2020 April 28, Insight-HXMT has implemented a dedicated observation on the magnetar SGR J1935+2154. Thanks to the wide energy band (1–250 keV) and high sensitivity of Insight-HXMT, we obtained 75 bursts from SGR J1935+2154 during a month-long activity episode after the emission of FRB 200428. Here we report the detailed time-integrated spectral analysis of these bursts and the statistical distribution of the spectral parameters. We find that for  $\sim 15\%$  (11/75) of SGR J1935+2154 bursts, the CPL model is preferred, and most of them occurred in the later part of this active epoch. In the cumulative fluence distribution, we find that the fluence of bursts in our sample is about an order of magnitude weaker than that of Fermi/GBM, but it follows the same power-law distribution. Finally, we find a burst with similar peak energy to the time-integrated spectrum of the X-ray burst associated with FRB 200428 (FRB 200428-Associated Burst), but the low energy index is harder.

*Unified Astronomy Thesaurus concepts:* [Magnetars \(992\)](#)

## 1. Introduction

Magnetars are a group of neutron stars with extremely strong magnetic fields ( $\sim 10^{14}$ – $10^{15}$  G; Thompson & Duncan 1995). They are usually identified with long spin periods ( $\sim 2$ – $12$  s) and fast spin-down rates ( $\sim 10^{-13}$ – $10^{-11}$  s s<sup>-1</sup>; Kouveliotou et al. 1998; Olausen & Kaspi 2014). Some special emission phenomena show strong connections with magnetars, including soft gamma repeaters (SGRs) and anomalous X-ray pulsars (AXPs). In fact, those unpredictable soft gamma-ray or hard X-ray bursts have been detected from more than two-thirds of the magnetar population (Olausen & Kaspi 2014).<sup>7</sup> Based on the duration and the peak luminosity, these soft gamma-ray bursts can be classified into three categories. Giant flares are the most energetic and rarest events. They start with a subsecond hard spike that is brighter than  $10^{44}$  erg s<sup>-1</sup>, followed by the emission decay lasting for several minutes (Mazets et al. 1979; Hurley et al. 1999; Palmer et al. 2005; Roberts et al. 2021). Intermediate flares present broader peaks (1–40 s), with a peak luminosity of  $10^{41}$ – $10^{43}$  erg s<sup>-1</sup> (Turolla et al. 2015). Short bursts are the most common ones. Typically they last for  $\sim 0.1$ – $1$  s and have a peak luminosity of  $10^{39}$ – $10^{41}$  erg s<sup>-1</sup> (Turolla et al. 2015).

As important clues for understanding the emission mechanism, the spectral properties of magnetar bursts have been

extensively studied. Our knowledge of the burst spectrum goes deeper thanks to X-/gamma-ray telescopes that are sensitive to a broad energy range. Using Fermi/GBM data (8–200 keV), Lin et al. (2011) found that the cutoff power-law model (COMPT) and the sum of two blackbody functions (BB+BB) can describe the burst spectrum equally well for magnetar SGR J0501+4501. Similar results are also reported for other magnetars (e.g., van der Horst et al. 2012; Collazzi et al. 2015). However, these two spectral models have distinct implications: The BB+BB model indicates that photons come from thermalized plasma, while COMPT points to the opposite direction. Occasionally, some bursts are detected by both soft X-ray and gamma-ray telescopes, enabling a joint broader-band spectral analysis (e.g., 1–200 keV), which statistically prefers the BB+BB model in most cases (Israel et al. 2008; Lin et al. 2012). Unfortunately, the vast majority of magnetar bursts were not observed in such a broad energy range; thus, whether their spectra are thermal or nonthermal is somewhat debatable.

SGR J1935+2154 was discovered by the Swift/Burst Alert Telescope (BAT) on 2014 July 5 (Stamatikos et al. 2014). It was confirmed as a magnetar with a spin period  $P = 3.25$  s and spin-down rate  $\dot{P} = 1.43 \times 10^{-11}$  s s<sup>-1</sup> (Israel et al. 2016). Since its discovery, SGR J1935+2154 has experienced at least seven outbursts in 2014, 2015, 2016 (two), 2019, 2020, and 2021 (Younes et al. 2017; Lin et al. 2020a, 2020b), making it the most prolific magnetar. During its active episode in 2020, a fast radio burst (FRB 200428) was detected from the general direction of SGR J1935+2154 by CHIME and STARE2 (Bochenek et al. 2020; CHIME/FRB Collaboration et al. 2020). At the dispersion-corrected burst time of FRB 200428, a

<sup>7</sup> <http://www.physics.mcgill.ca/pulsar/magnetar/main.html>



hard X-ray burst from SGR J1935+2154 was detected by Insight-Hard X-ray Modulation Telescope (Insight-HXMT hereafter; Li et al. 2021), INTEGRAL (Mereghetti et al. 2020), Konus-Wind (Ridnaia et al. 2021), and AGILE (Tavani et al. 2021). Thanks to the accurate localization provided by Insight-HXMT and INTEGRAL (Mereghetti et al. 2020; Li et al. 2021), this hard X-ray burst provides unambiguous evidence that FRB 200428 originates from the Galactic magnetar SGR J1935+2154. Moreover, we first suggested that these two narrow peaks of this hard X-ray burst, consistent with these two radio pulses of FRB 200428, is probably the high-energy counterpart of FRB 200428 (Li et al. 2021).

On the contrary, FAST unveiled a rare connection between magnetar X-ray bursts and fast radio bursts (FRBs) by placing the most stringent radio upper limit on 29 X-ray bursts from SGR J1935+2154 shortly before FRB 200428 (Lin et al. 2020c). The reason for missing radio emission of magnetar X-ray bursts is unclear. It can be intrinsic (e.g., the X-ray burst associated with FRBs is atypical) or due to some selection effects (e.g., beaming effects or narrow bandwidth of FAST) or both (Lin et al. 2020c). Nevertheless, using Insight-HXMT data in the wide energy range of 1–250 keV, Li et al. (2021) confirmed that the X-ray burst associated with FRB 200428 (denoted as FRB 200428-Associated Burst hereafter) prefers a nonthermal origin, while the spectrum of a typical magnetar burst is more thermalized or curved in a similar energy range (Lin et al. 2012; Younes et al. 2021). Therefore, multi-wavelength observations of active magnetars are crucial to expand the sample of the FRB and magnetar X-ray burst association pairs and to deepen the understanding of the physics behind the SGR–FRB connection.

The discovery of the X-ray burst associated with FRB 200428 demonstrated that Insight-HXMT, with a broad energy coverage (1–250 keV) and high sensitivity, is very capable of exploring the SGR–FRB relation and constraining the emission properties of magnetar bursts. It also motivated a dedicated long Target of Opportunity (ToO) observation to continuously monitor SGR J1935+2154 until its bursting activity ceased. Complimented by other gamma-ray burst monitors (e.g., Fermi/GBM), Insight-HXMT provided the most complete monitoring coverage of SGR J1935+2154 bursts after the emission of FRB 200428.

From this 33 day dedicated observation of Insight-HXMT, we identified 75 bursts ( $\sim 90\%$  of all bursts detected from SGR J1935+2154 during this period) in the exposure time of 1.65 Ms, as described in the first paper of this special series (Cai et al. 2022, hereafter Paper I). This is an exceptional burst sample with a broad energy range (1–250 keV), which could enable detailed studies of the burst properties and the search for a potential association between SGR bursts and FRBs.

In order to investigate how special the FRB 200428-Associated Burst is in terms of its nonthermal spectrum and whether SGR J1935+2154 is unique or not among the SGR population, we analyzed the spectra of the 75 bursts detected by Insight-HXMT during this dedicated ToO observation, which are presented in detail in this paper.

## 2. Observations

### 2.1. Instrument

As China’s first X-ray astronomy satellite launched on 2017 June 15, Insight-HXMT (Zhang et al. 2018, 2019; Li et al. 2020)

consists of three telescopes: the High Energy X-ray telescope (HE) covering the energies of 20–250 keV (Liu et al. 2019), the Medium Energy X-ray telescope (ME) with energies of 5–30 keV (Cao et al. 2019), and the Low Energy X-ray telescope (LE) in 1–15 keV (Chen et al. 2019). The time resolutions of LE, ME, and HE are 0.98 ms, 255  $\mu$ s, and less than 10  $\mu$ s, respectively. The energy resolutions of LE, ME, and HE are  $\sim 2.4\%$  at 5.9 keV,  $\sim 16.9\%$  at 17.8 keV, and  $\sim 15\%$  at 60 keV (Cao et al. 2019; Chen et al. 2019; Liu et al. 2019), respectively. For HE, data from 17 NaI detectors (rather than a CsI detector) are used to do spectral analysis, whereas the blind NaI detector is used for background modeling (Liu et al. 2019).

### 2.2. Burst Sample

About 13 hr after the first Fermi/GBM and Swift/BAT trigger of a burst from SGR J1935+2154 on 2020 April 27, Insight-HXMT launched a 33 day dedicated ToO monitor campaign of this source. This observation covered from April 28 07:14:51 to April 29 12:02:36 and from April 30 06:58:23 to June 1 00:00:01 (all times quoted in this paper are in UTC). Using a multidetector trigger method and a careful identification of fake bursts from instrumental effects and other sources (see Paper I for details), we found 75 short bursts from SGR J1935+2154 (Paper I). In this burst sample, the LE data are filtered out owing to the bright Earth for 14 bursts, whereas both the LE and ME data are lost on board for one burst (burst #67). Seven bright bursts suffer from data saturation (i.e., data loss caused by a huge amount of data in a short time period) in HE or LE, while ME does not have the data saturation issue.

Because the majority of bursts, including the burst forests (Kaneko et al. 2021), are concentrated in the first  $\sim 10$  hr of this episode (Lin et al. 2020b), which is before the Insight-HXMT ToO observation, the number of bursts found in this Insight-HXMT observation is not as large as that reported by Lin et al. (2020b) and Younes et al. (2020), which monitored the source in a more active episode with Fermi/GBM and NICER, respectively. However, Insight-HXMT has a higher sensitivity and broader energy range coverage for hard X-ray bursts and thus provides a unique data set for this 33 day observation embracing FRB 200428. Among 75 bursts detected by Insight-HXMT, only seven bright bursts were jointly detected by Fermi/GBM.

## 3. Spectral Analysis Method

### 3.1. Spectral Models

For consistency with the previous spectral analyses of the FRB 200428-Associated Burst of Insight-HXMT (Li et al. 2021), we choose five different models to fit the spectra of bursts in our sample: (1) single power law (PL), (2) cutoff power law (CPL), (3) single blackbody (BB), (4) two blackbodies (BB+BB), (5) blackbody plus power law (BB+PL). All models are formulated in units of photon flux with energy ( $E$ ) in keV and multiplied by a normalization factor  $N$  in units of photons  $\text{cm}^{-2} \text{s}^{-1} \text{keV}^{-1}$ .

1. *PL*: A simple photon power law with photon index of  $\alpha$  and normalization of  $N$ ,

$$f_{\text{PL}}(E) = NE^{-\alpha}. \quad (1)$$

2. *CPL*: A power law with a high-energy exponential roll-off parameterized by power-law photon index  $\alpha$ ,  $e$ -folding energy of exponential roll-off (in keV)  $E_{\text{cut}}$ ,

and normalization  $N$ ,

$$f_{\text{CPL}}(E) = NE^{-\alpha} \exp\left(-\frac{E}{E_{\text{cut}}}\right). \quad (2)$$

In this model, the peak energy ( $E_{\text{peak}}$ ) in the  $\nu F_\nu$  spectrum is defined as

$$E_{\text{peak}} = E_{\text{cut}}(2 - \alpha). \quad (3)$$

3. *BB*: A blackbody spectrum with normalization proportional to the surface area parameterized with temperature  $kT$  (in keV) and normalization  $K$ ,

$$f_{\text{BB}}(E) = \frac{K \times 1.0344 \times 10^{-3} E^2}{\exp(E/kT) - 1}, \quad (4)$$

$$K = \frac{R_{\text{km}}^2}{D_{10}^2}, \quad (5)$$

where  $R_{\text{km}}$  is the radius in km of the blackbody emission region and  $D_{10}$  is the distance to the source in units of 10 kpc.

In addition, a *wabs* model is used to account for the absorption effect of the interstellar medium. The equivalent hydrogen column in the model for interstellar absorption could not be constrained well owing to the low flux in the majority bursts of this sample. Therefore, we fix the interstellar absorption term ( $N_{\text{H}}$ ) to  $2.79 \times 10^{22} \text{ cm}^{-2}$  in the following analyses,<sup>8</sup> which is the best-fit value derived from the bright FRB 200428-Associated Burst (Li et al. 2021).

### 3.2. Spectral Analysis Procedure

The spectral analysis of the burst sample is based on the Insight-HXMT 1L data using the current version (v2.04) of the Insight-HXMT Data Analysis Software package (*HXMTDAS*).<sup>9</sup> We generate the spectra using the commands *hespecgen*, *mespecgen*, and *lespecgen*. The time-integrated spectra are derived jointly using HE, ME, and LE data, excluding the blinded detector unit of HE, ME, and LE and the wide field of view (FOV) detector unit of ME and LE. The data of 1–10 keV with LE, 10–30 keV with ME, and 28–250 keV with HE are used to fit the spectra. There are some bursts for which the LE or ME data are not available owing to bright Earth or data loss, so only the HE data or HE and ME data are used to fit their spectra. The time-integrated burst spectra are extracted for the burst duration derived from the Bayesian block method ( $T_{\text{bb}}$ ), which is the common burst interval of all three telescopes (see Paper I for details).<sup>10</sup> For weak bursts, the *GRPPHA* command<sup>11</sup> is used to group the observed data (e.g., GROUP MIN RCNTS) to ensure sufficient statistics. The background spectra are accumulated from the data events during the pre- and post-burst time intervals (i.e., from  $T_0 - 7$  s to  $T_0 - 2$  s and from  $T_0 + 2$  s to  $T_0 + 7$  s, where  $T_0$  is the trigger time of the burst).

We perform spectral fitting with Xspec 12.11.1 using Cash statistics (C-stat; Cash 1979). We call a model ( $M_1$ ) an adequate fit when all model parameters fall in the physically meaningful region with a confidence level of no less than  $1\sigma$

(e.g.,  $kT$ ,  $E_{\text{cut}}$ , and normalization are positive). To identify which model can better describe the spectrum, we calculate the Bayesian information criterion (BIC) for each spectral model as presented in Kaneko et al. (2021). A smaller BIC indicates that the model fits the data better. If the reduction in BIC is more than 10, then the model with a smaller value is considered to be significantly better than the other one. Therefore, for one burst, we may have either a significantly preferred model or more than one adequate model. We calculate the unabsorbed fluence and flux using the parameters of the model with the smallest BIC.

There are six bursts in our sample that suffered from the data saturation problem (FRB200428-Associated Burst excluded), which means that some of the events cannot be recorded. The data loss is due to the limited transmission bandwidth. But for each of them, at least one telescope is free from the saturation. Therefore, we multiply a constant by the spectral models during the spectral fitting process in order to correct the saturation effect (e.g., *const \* wabs \* (bb + bb)* in Xspec). This constant parameter represents the relative data loss ratio. We fix the constant at 1 for the telescopes that are not affected by the saturation and leave it free for others.

There are seven bursts in our catalog jointly observed by Insight-HXMT and Fermi/GBM. In order to verify our spectral analysis and compare between different instruments, we perform a joint spectral analysis using both data. We extract burst spectra using data of NaI detectors of GBM with an angle to the source less than  $30^\circ$ . The integration time of each burst spectrum is the maximum burst interval of the two instruments. We also include a multiplicative factor to account for the systematic difference between these two instruments.

## 4. Results

### 4.1. Spectral Results of the Burst Sample

Following the spectral fitting methods mentioned above, we did the spectral fitting with five spectral models to the Insight-HXMT data of 75 bursts from SGR J1935+2154. The trigger time, adequately fit spectral model parameters, fit statistics, and unabsorbed flux in 1–250 keV of each burst, as well as their  $1\sigma$  errors, are listed in Table 4. Our fit results of the FRB 200428-Associated Burst agree with those reported in Li et al. (2021). We list the published results in Table 4. Figure 1 presents the burst spectra of a saturated burst and an unsaturated burst in the left and right panels, respectively. The relative data loss ratio of HE data is  $\sim 39\%$  of the saturated burst, while LE and ME data of this burst are not affected by the saturation and their constants are fixed at 1.

We summarize the results of different models in Table 1. The number of bursts that can be adequately fit with CPL, BB+BB, BB+PL, PL, and BB models is 30, 26, 19, 33, and 19, respectively, while the number of bursts that can be best fit with CPL, BB+BB, BB+PL, PL, or BB is 11, 3, 1, 18, and 9, respectively. We note that  $\sim 15\%$  (11/75) of the bursts in our sample can be best fit with the CPL model and  $\sim 24\%$  (18/75) can be best fit with the PL model, which means that these bursts do not contain a significant BB component. Meanwhile, some bursts are equally well described by two or more models. For those bursts, we select the model with the minimum BIC value to calculate the burst flux and fluence. The number of bursts with the CPL, BB+BB, BB+PL, PL, or BB model

<sup>8</sup> The results do not change significantly when varying the  $N_{\text{H}}$ .

<sup>9</sup> <http://www.hxmt.cn/>

<sup>10</sup> We note that performing spectral analysis in the total burst duration of all three telescopes does not alter any of our main conclusions.

<sup>11</sup> <https://heasarc.gsfc.nasa.gov/ftools/>

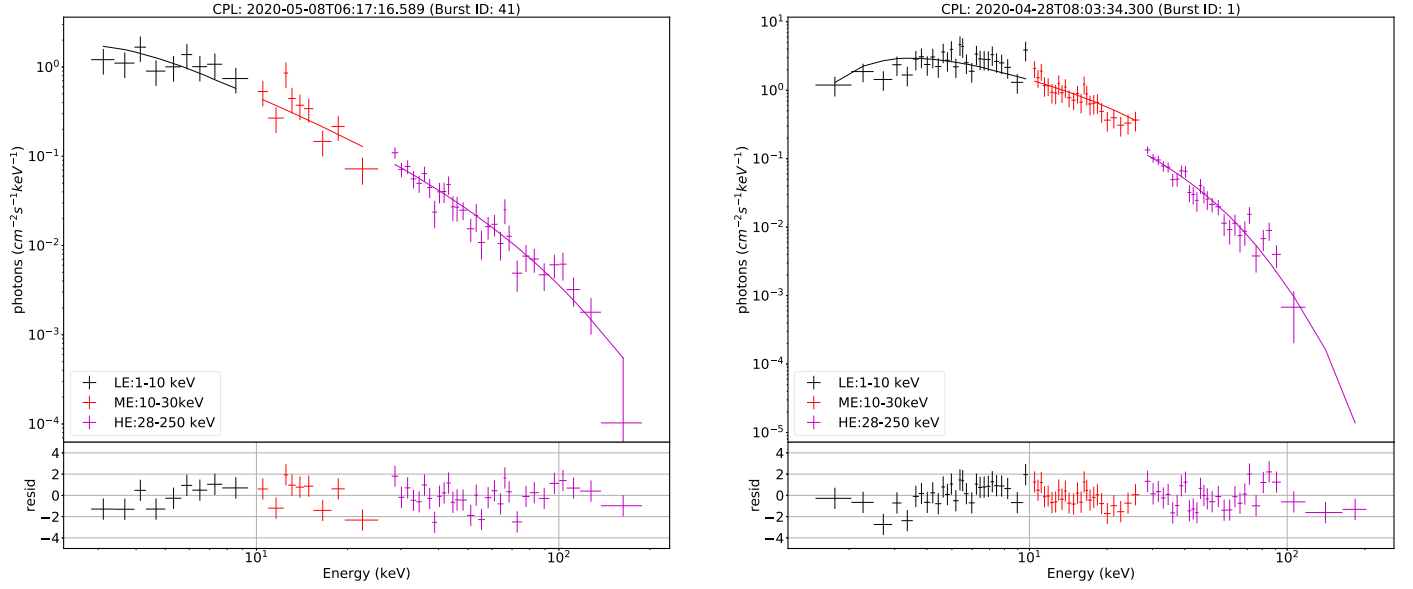


**Figure 1.** The spectra of an unsaturated burst (left panel) and a saturated burst (right panel) from SGR J1935+2154 observed by Insight-HXMT. These spectra are fitted with the CPL model in the energy band of 1–250 keV. The lower panels show the fit residuals. For the burst that suffered saturation in the HE telescope, the flux normalization parameter ( $f$ ) of HE is allowed to vary, while those of ME and LE are frozen to be 1 during the fit.

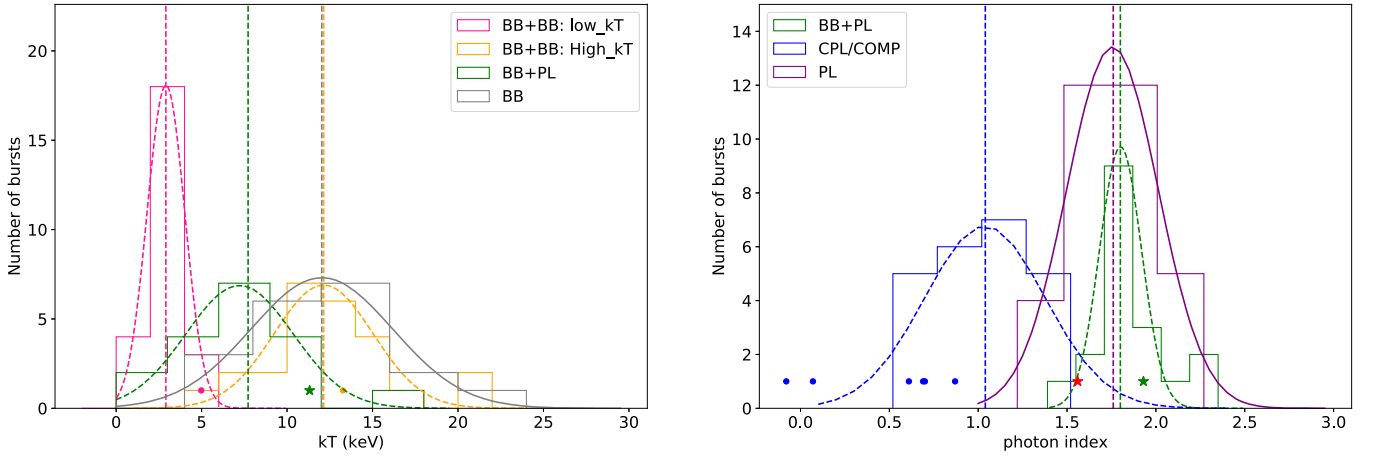


**Figure 2.** Left: distributions of the BB temperatures derived with the BB+BB (pink and orange represent low and high BB temperatures, respectively), BB+PL (green), and BB (gray) models. Right: distributions of the photon index of BB+PL (green), CPL (blue), and PL (purple) models. The circles and stars in both panels represent the saturated bursts and the FRB 200428-Associated Burst with different models, respectively. The green and red stars are the FRB 200428-Associated Burst with the BB+PL model and CPL model, respectively. The FRB 200428-Associated Burst is labeled as red star in all figures in this paper.

**Table 1**  
Summary of Spectral Models Employed in Fitting SGR J1935+2154 Burst Spectra

Samples	Number of Bursts	CPL <sup>b</sup>	BB+BB <sup>b</sup>	BB+PL <sup>b</sup>	PL <sup>b</sup>	BB <sup>b</sup>
Unsaturated	68	23 (4)	25 (3)	18 (0)	33(18)	19 (9)
Saturated	6	6 (6)	1 (0)	0	0	0
FRB 200428-Associated <sup>a</sup>	1	1 (1)	0	1 (1)	0	0
All	75	30 (11)	26 (3)	19 (1)	33 (18)	19 (9)

**Notes.**

<sup>a</sup> The X-ray burst associated with FRB 200428.

<sup>b</sup> The number of bursts whose adequate (preferred) model is CPL, BB+BB, BB+PL, PL, and BB, respectively.

having minimum BIC values is 24, 13, 3, 22, and 13, respectively.

For those 26 bursts, including one saturated, adequately fit by the BB+BB model, we study the characteristics of two BB

components. The left panel of Figure 2 shows the distributions of temperatures of the low (pink) and high (orange) BB components. The low and high temperatures follow a Gaussian trend with a mean value of  $\sim 2.91$  and  $\sim 12.14$  keV,



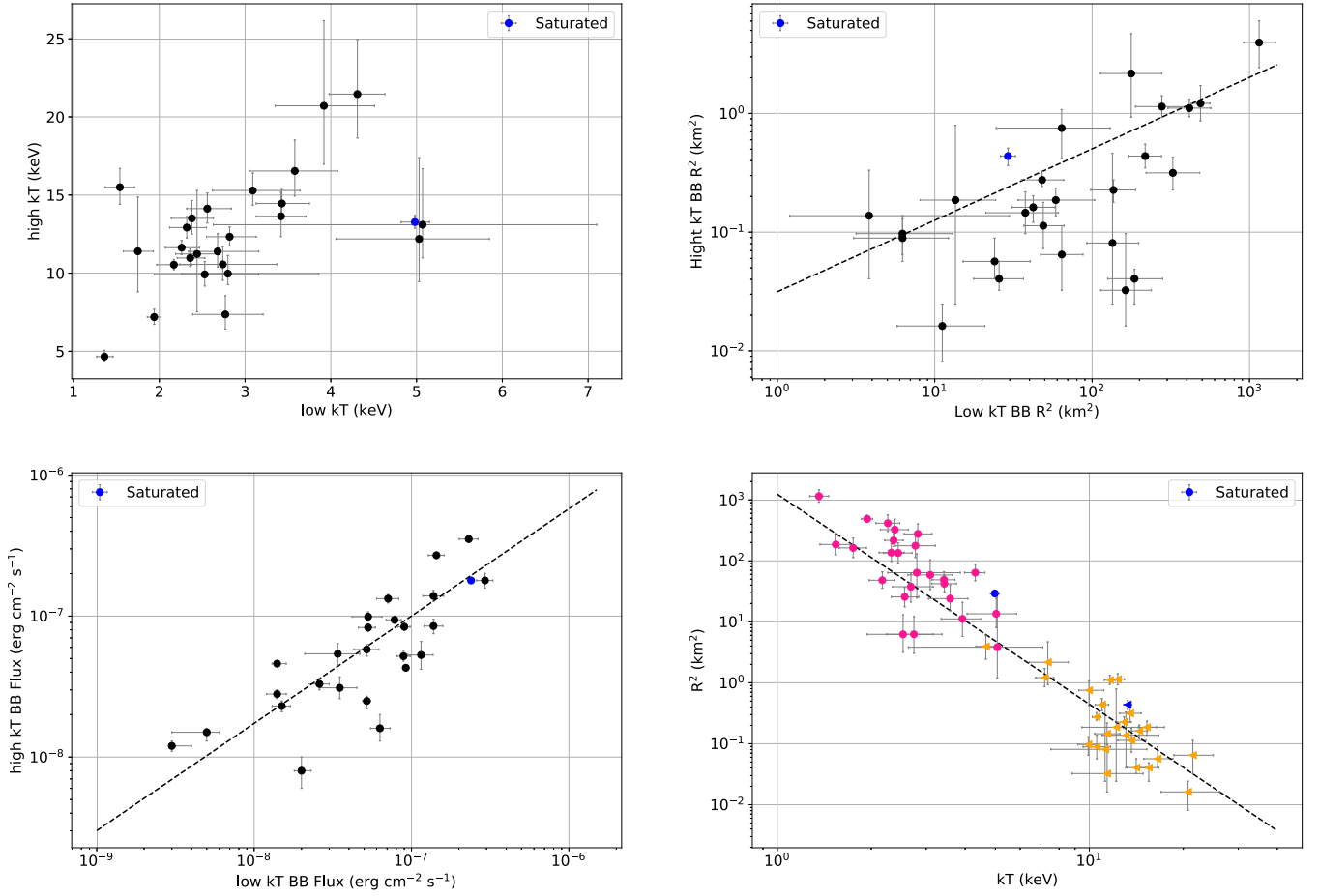


**Figure 3.** Top left: relation between  $kT$  of the two BB components in the BB+BB model. Top right: correlations of the radius of BB emission regions of the two BB components in the BB+BB model. Bottom left: the flux of both BB components, measured in the 1–250 keV energy band. Bottom right: the emission areas ( $R^2$ ) as a function of the low (pink circles) and high (orange triangle) BB temperatures. The blue circles and black dashed lines of those panels represent the saturated bursts and the PL fit of both BB components.

**Table 2**

Results of the Gaussian Fits to the Spectral Parameter Distributions of SGR J1935+2154 Bursts

Model	Parameter	$\mu^a$	$\sigma^b$
BB	$kT$ (keV)	$12.03 \pm 0.33$	$4.15 \pm 0.27$
PL	Photon index	$1.76 \pm 0.01$	$0.26 \pm 0.01$
CPL	Photon index	$1.04 \pm 0.07$	$0.34 \pm 0.06$
BB+BB	$kT_{\text{low}}$ (keV)	$2.91 \pm 0.003$	$1.10 \pm 0.001$
BB+BB	$kT_{\text{high}}$ (keV)	$12.14 \pm 0.37$	$2.90 \pm 0.30$
BB+PL	$kT$ (keV)	$7.72 \pm 0.39$	$3.13 \pm 0.32$
BB+PL	Photon index	$1.80 \pm 0.02$	$0.12 \pm 0.01$

**Notes.**

<sup>a</sup> The mean value of the Gaussian fit.

<sup>b</sup> The error of the Gaussian fit.

respectively. The best-fit parameters of the Gaussian fit are listed in Table 2. We find no correlation between the temperatures of two BB components (top left panel of Figure 3). The emission area of each BB component can be calculated from the normalization of the spectral fit by assuming that SGR J1935+2154 is 9 kpc away.

We study the correlations between parameters of the two BB components. In order to quantify the significance of the correlation, we perform the Spearman’s rank order correlation test. We consider a correlation significant if the chance probability  $P < 5.7 \times 10^{-7}$  (about  $5\sigma$  in a normal distribution). If the chance probability  $5.7 \times 10^{-7} < P < 2.7 \times 10^{-3}$  (about  $3\sigma$ ), then the correlation is marginally significant (van der Horst et al. 2012). We further fit a power-law model to the data points of significant and marginally significant correlations,<sup>12</sup> and we present results of the Spearman test and the PL fit in Table 3. The emission areas of hot and cool BBs are marginally correlated. The flux of the cool BB is significantly correlated with that of the hot BB (bottom left panel of Figure 3). As presented in the bottom right panel of Figure 3, for each BB component, the emission area is marginally anticorrelated with the temperature. The power-law indices of these two trends are consistent within errors. We further fit a power-law model to the data points of two BB components, which yields a power-law index of  $-3.45 \pm 0.23$ .

There are 30 bursts with the CPL model as the adequate fitting, seven of which are saturated owing to their brightness. The photon index ( $\Gamma$ ) distribution of the CPL model is shown in the right panel of Figure 2 (see blue lines), for which the Gaussian mean value is  $1.04 \pm 0.07$  (Table 2). The  $E_{\text{peak}}$  and

<sup>12</sup> The PL fit is obtained from linear fitting in logarithmic scale.

**Table 3**

Results of Power-law (PL) Fits to Parameter Correlations and Spearman Test Results of the Correlations

Correlation <sup>a</sup>	PL Fit Index ( $\alpha$ )	Correlation Coefficient ( $\rho$ )	Chance Probability ( $P$ )
$R_{\text{high}}^2 \propto (R_{\text{low}}^2)^\alpha$	$0.60 \pm 0.10$	0.56	$2.00\text{E}-03$
$F_{\text{high}} \propto (F_{\text{low}})^\alpha$	$0.74 \pm 0.09$	0.84	$1.09\text{E}-08$
$R_{\text{low}}^2 \propto (kT_{\text{low}})^\alpha$	$-3.11 \pm 0.68$	-0.64	$4.74\text{E}-04$
$R_{\text{high}}^2 \propto (kT_{\text{high}})^\alpha$	$-3.24 \pm 0.60$	-0.60	$1.42\text{E}-03$
$R^2 \propto (kT)^\alpha$	$-3.45 \pm 0.23$	-0.90	$5.10\text{E}-20$

**Note.**<sup>a</sup>  $R^2$ ,  $F$ , and  $kT$  are the emitting area, flux, and temperature of a BB component, respectively.

$E_{\text{cut}}$  distributions are shown in Figures 4 and 5, respectively. The peak energy ( $E_{\text{peak}}$ ) ranges from 12.78 to 50.32 keV, with an average of 33.56 keV, while the  $E_{\text{cut}}$  range is from 9.20 to 81.80 keV, with an average value of 35.70 keV. We find that there are no significant correlations between photon index ( $\alpha$ ) and  $E_{\text{cut}}$  with burst flux or fluence (see Figures 6 and 7). There are also no clear correlations between  $E_{\text{peak}}$  and burst flux or fluence, which are shown in Figure 8.

For 19 bursts with the adequate model of BB+PL, the distributions of the BB+PL model parameters are shown in Figure 2. The BB temperature and photon index of the BB+PL model follow a Gaussian distribution with the best-fit mean values of  $7.72 \pm 0.39$  keV and  $1.80 \pm 0.02$ , respectively (see Table 2).

Finally, some bursts in our sample can be adequately fit with simple models (i.e., BB or PL). The mean temperature for 19 bursts with the BB model is  $11.75 \pm 0.71$  keV, and the mean photon index for 33 PL bursts is  $1.76 \pm 0.02$  (see Figure 2). These values with their statistical errors are also shown in Table 2. We note that those bursts that can be fit better with simple models are quite dim, with the highest fluence being about  $2.5 \times 10^{-8}$  erg cm<sup>-2</sup>. Interestingly, we find that the photon index of the simple PL model is similar to the PL index of the BB+PL model, and the temperature  $kT$  of the simple BB model is similar to the high temperature of the BB+BB model.

#### 4.2. Joint Spectral Fit

In Figure 9, we present an example of the joint spectral analysis of Fermi/GBM and Insight-HXMT. We first analyze the joint spectrum in 8–200 keV. Our results are consistent with the spectral fit with GBM-only data within the  $1\sigma$  confidence level (Lin et al. 2020b). The constants of GBM, HE, ME, and LE are 0.82, 0.83, 1, and 1, respectively, for the CPL fit in 8–200 keV; the constants of GBM, HE, ME, and LE are 0.84, 0.94, 1, and 1, respectively, for the BB+BB fit in 8–200 keV. The difference between HE and LE/ME is due to a saturation effect. In the narrow energy range, if only using the GBM data, the BIC value of the CPL model fit is smaller than the BIC of the BB+BB model. However, the difference is not enough to conclude that CPL is significantly preferred. We also fit the joint spectrum in 1–250 keV. The model parameters agree with the values listed in Table 4, while being quite different from the results from the narrow energy band fit. The model parameters (e.g., photon index,  $E_{\text{cut}}$ , low and high temperature) of the broader band are smaller than those of the narrow band (see Figure 9 for more details). Moreover, using data in the broader

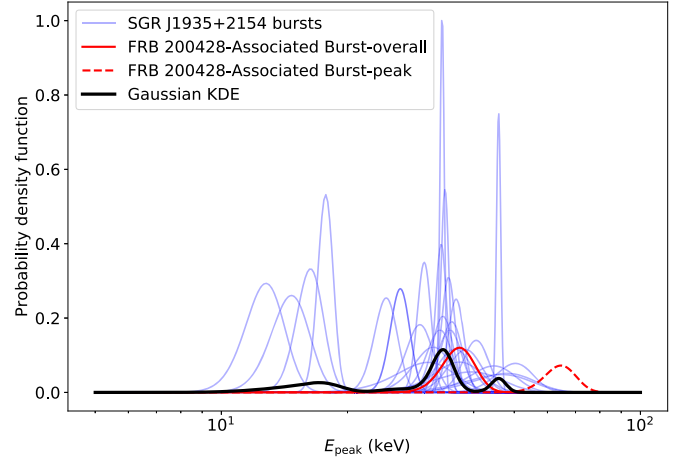


**Figure 4.** The distribution of  $E_{\text{peak}}$  of the CPL model for 29 bursts and comparison to the FRB 200428-Associated Burst. The blue lines are the probability density function (pdf) of  $E_{\text{peak}}$ . The black line represents the pdf of a Gaussian kernel for the pdfs of 29 bursts. The red solid line (time-averaged spectrum from  $T_0 - 0.2$  s to  $T_0 + 1.0$  s) and dashed line (peak spectrum from  $T_0 + 0.41$  s to  $T_0 + 0.47$  s) are the pdfs of the  $E_{\text{peak}}$  of the FRB 200428-Associated Burst as measured with Insight-HXMT (see supplementary Tables 4 and 6 in Li et al. 2021 for more details).

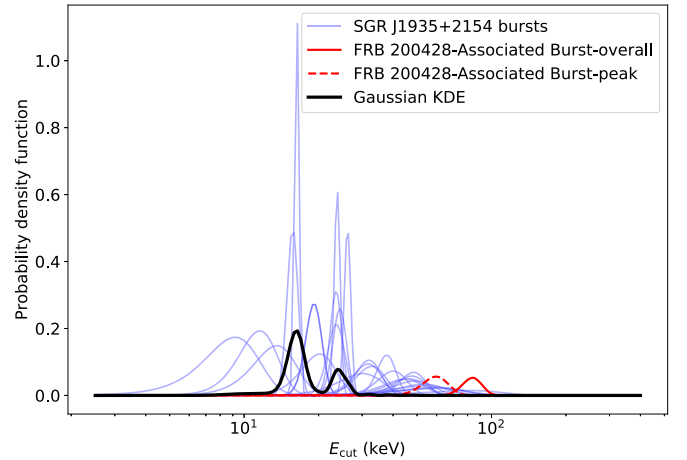


**Figure 5.** The distribution of  $E_{\text{cut}}$  derived with the CPL model for 29 bursts and comparison to the FRB 200428-Associated Burst. The red line is the pdf of  $E_{\text{cut}}$  of the FRB 200428-Associated Burst as measured with Insight-HXMT (Li et al. 2021). Other captions are the same as Figure 4.

energy range, the CPL model is significantly preferred over the BB+BB model with a reduction of 139 in the BIC value.

The above facts demonstrate that the cross-calibration of energy responses between Insight-HXMT and Fermi/GBM in the common energy range (i.e., 8–200 keV) is adequate and the low energy band (i.e., 1–10 keV) of Insight-HXMT plays an important role in determining the spectral shape.

#### 5. Discussion

As shown above, we have analyzed the time-integrated spectral properties of 75 bursts from SGR J1935+2154 observed with Insight-HXMT. The fluence of this burst sample ranges from  $8 \times 10^{-10}$  erg cm<sup>-2</sup> to  $3.46 \times 10^{-6}$  erg cm<sup>-2</sup> in the energy range of 8–200 keV, with the minimum fluence about an order of magnitude dimmer than that of observations by Fermi/GBM or Swift/BAT (e.g., Lin et al. 2020a, 2020b). The total fluence emitted in our burst sample is  $6.81 \times 10^{-6}$  erg cm<sup>-2</sup> (8–200 keV), corresponding to  $6.57 \times 10^{40}$  erg (for a distance of

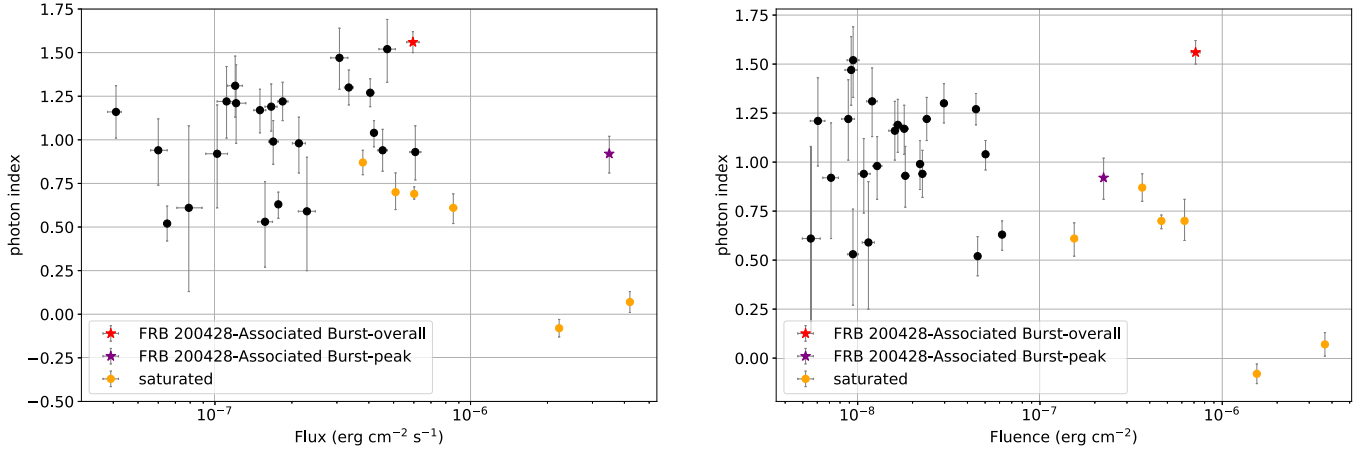


**Figure 6.** Left: scatter plot of the photon index and flux in 1–250 keV derived with the CPL model. Right: scatter plot of the photon index and fluence in 1–250 keV derived with the CPL model. The red and purple stars are the time-integral and peak spectra of FRB 200428-Associated Burst (Li et al. 2021), respectively. The orange circles represent the saturated bursts.

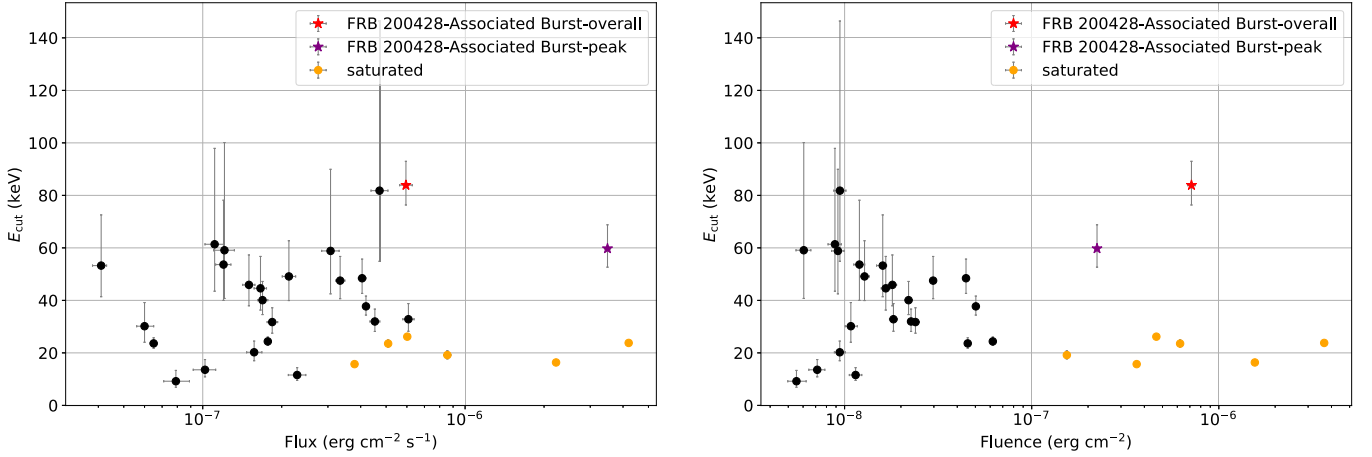


**Figure 7.** Left: scatter plot of  $E_{\text{cut}}$  and flux in 1–250 keV derived with the CPL model. Right: scatter plot of  $E_{\text{cut}}$  and fluence in 1–250 keV derived with the CPL model. The red and purple stars are the time-integral and peak spectra of FRB 200428-Associated Burst (Li et al. 2021), respectively. The orange circles represent the saturated bursts.

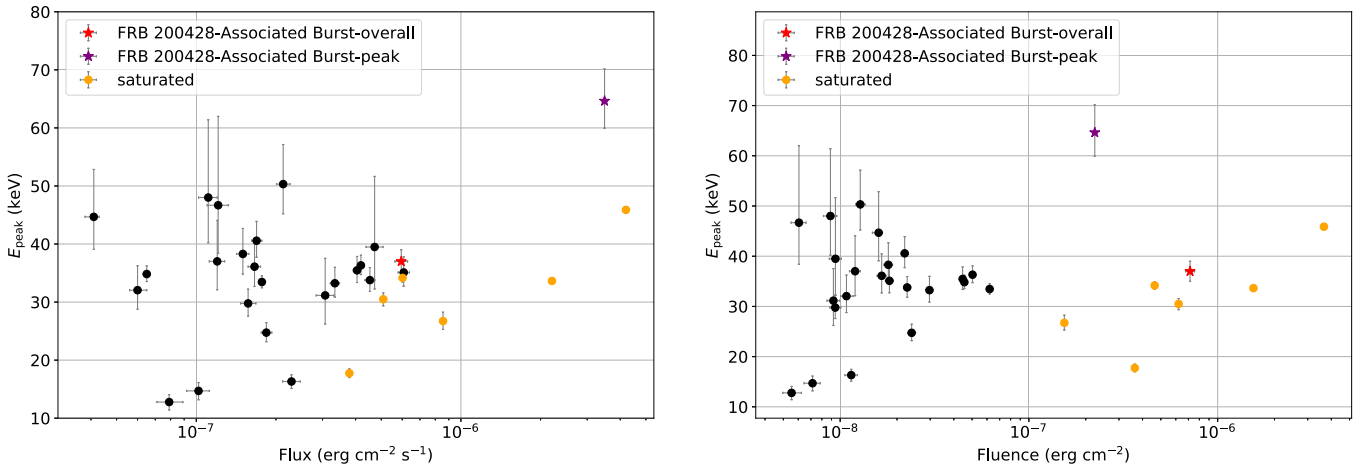


**Figure 8.** Left: scatter plot of the  $E_{\text{peak}}$  and flux in 1–250 keV derived with the CPL model. Right: scatter plot of the  $E_{\text{peak}}$  and fluence in 1–250 keV derived with the CPL model. The red and purple stars are the time-integral and peak spectra of FRB 200428-Associated Burst (Li et al. 2021), respectively. The orange circles represent the saturated bursts.

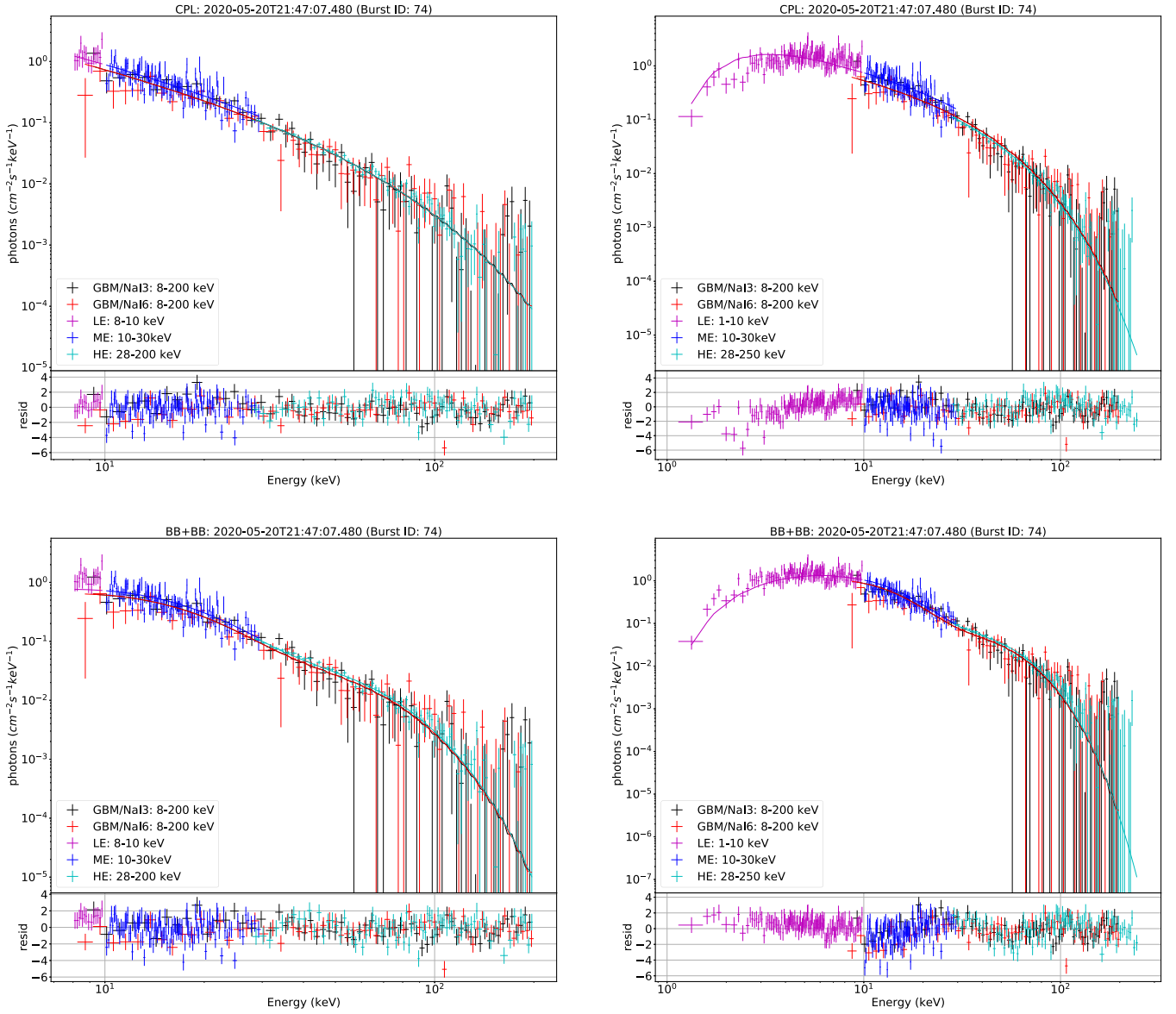


**Figure 9.** The Insight-HXMT and Fermi/GBM joint spectral analysis of SGR J1935+2154 bursts. Data from HE, ME, and LE of Insight-HXMT and NaI detector #3 and #6 of Fermi/GBM are used. An interstellar absorption parameter of  $2.79 \times 10^{22} \text{ cm}^{-2}$  is adopted. Left: Insight-HXMT and Fermi/GBM data in the same energy range of 8–200 keV are used in the joint spectral analysis. The CPL model fit ( $\alpha = 1.34 \pm 0.07$ ,  $E_{\text{cut}} = 37.28 \pm 2.44 \text{ keV}$ , and  $\text{C-Stat/dof} = 642.18/337$ ) is shown in the top left panel, while the BB+BB fit ( $kT_{\text{low}} = 4.31 \pm 0.09 \text{ keV}$ ,  $kT_{\text{high}} = 13.80 \pm 0.26 \text{ keV}$ , and  $\text{C-Stat/dof} = 714.18/336$ ) is shown in the bottom left panel. Right: Insight-HXMT data in 1–250 keV and Fermi/GBM data in 8–200 keV are used in the joint spectral analysis. The CPL model fit ( $\alpha = 0.73 \pm 0.04$ ,  $E_{\text{cut}} = 25.14 \pm 0.70 \text{ keV}$ , and  $\text{C-Stat/dof} = 900.34/451$ ) is shown in the top right panel, while the fit with the BB+BB model ( $kT_{\text{low}} = 3.34 \pm 0.05 \text{ keV}$ ,  $kT_{\text{high}} = 12.31 \pm 0.15 \text{ keV}$ , and  $\text{C-Stat/dof} = 1032.75/450$ ) is shown in the bottom right panel.

9 kpc). The FRB 200428-Associated Burst is brighter than  $\sim 96\%$  (72/75) of the events in our sample.

### 5.1. Comparison of Burst Spectra with Those of GBM

The parameters of the CPL and BB+BB models derived from Insight-HXMT are somewhat different from those of the GBM observations. We find that the mean temperature of the harder BB component ( $\sim 12.14 \text{ keV}$ ) is consistent with the results from GBM observations during 2020, while the mean temperature of the softer BB component ( $\sim 2.91 \text{ keV}$ ) is lower than that of GBM ( $\sim 4.50 \text{ keV}$ ; Lin et al. 2020b). The mean value of the spectral photon index is  $\sim 1.04$ , softer than the index measured by GBM ( $\sim 0.10$ ), and the average  $E_{\text{peak}}$  is  $\sim 34.14 \text{ keV}$ , higher

than that measured by GBM ( $\sim 26.30 \text{ keV}$ ; Lin et al. 2020b). Such differences could be caused by the evolution of the spectral properties of bursts from SGR J1935+2154. However, as shown in Section 4.2 of Insight-HXMT, the spectral parameters derived from the boarder band (1–250 keV) are different from the results of the narrower band (8–200 keV). Therefore, the differences between the spectral parameters given by Insight-HXMT and Fermi/GBM are also likely due to the different energy ranges between these two instruments. Nevertheless, there is no doubt that wide energy bandwidth is very important to accurately measure the whole burst spectrum and the 1–10 keV data of Insight-HXMT are necessary to constrain the low-energy shape of the burst spectrum of SGR J1935+2154.



**Table 4**  
SGR J1935+2154 Burst List Detected by Insight-HXMT

Burst Information		CPL or PL			BB+BB or BB			BB+PL			Two Components		Selected Model <sup>e</sup>
ID	Trigger Time (UTC)	$\Gamma$	$E_{\text{peak}}$ (keV)	C-Stat/dof <sup>a</sup>	$kT_{\text{low}}$ (keV)	$kT_{\text{high}}$ (keV)	C-Stat/dof <sup>b</sup>	$\Gamma$	$kT$ (keV)	C-Stat/dof <sup>c</sup>	$Flux_1^d$	$Flux_2^d$	
1 <sup>f</sup>	2020-04-28T08:03:34.300	$0.61^{+0.08}_{-0.09}$	$26.73^{+1.53}_{-1.43}$	91.1/79	...	...	...	...	...	...	$8.56^{+0.26}_{-0.26}$	...	CPL
2	2020-04-28T08:05:50.080	...	...	...	$1.94^{+0.08}_{-0.08}$	$7.19^{+0.5}_{-0.47}$	96.59/107	...	...	...	$0.92^{+0.04}_{-0.04}$	$0.43^{+0.02}_{-0.02}$	BB+BB
3	2020-04-28T08:14:45.985	$2.1^{+0.16}_{-0.17}$	...	22.99/21	$4.95^{+0.56}_{-0.49}$	...	28.93/21	...	...	...	$1.43^{+0.28}_{-0.24}$	...	PL
4	2020-04-28T09:08:44.280	$0.94^{+0.18}_{-0.2}$	$32.05^{+4.2}_{-3.28}$	85.97/87	$2.68^{+0.48}_{-0.34}$	$11.39^{+1.13}_{-1.0}$	89.5/86	$1.65^{+0.11}_{-0.12}$	$6.03^{+0.85}_{-0.67}$	86/86	$0.6^{+0.05}_{-0.04}$	...	CPL
5	2020-04-28T09:40:10.980	$0.61^{+0.47}_{-0.48}$	$12.78^{+1.28}_{-1.36}$	49.45/29	$2.44^{+0.26}_{-0.25}$	$11.23^{+4.06}_{-3.7}$	41.41/28	$1.72^{+0.27}_{-0.32}$	$2.57^{+0.34}_{-0.28}$	41.44/28	$0.63^{+0.1}_{-0.08}$	$0.16^{+0.04}_{-0.03}$	BB+BB
6	2020-04-28T09:46:05.300	...	...	...	$1.75^{+0.18}_{-0.17}$	$11.4^{+3.47}_{-2.59}$	29.19/30	...	...	...	$0.2^{+0.03}_{-0.02}$	$0.08^{+0.02}_{-0.02}$	BB+BB
7 <sup>h</sup>	2020-04-28T09:51:04.634	$0.87^{+0.07}_{-0.07}$	$17.74^{+0.76}_{-0.75}$	715.90/595	...	...	...	...	...	...	$3.79^{+0.06}_{-0.05}$	...	CPL
8	2020-04-28T09:51:39.394	$2.06^{+0.15}_{-0.16}$	...	10.08/13	...	...	...	...	...	...	$1.42^{+0.13}_{-0.13}$	...	PL
9	2020-04-28T10:54:23.850	...	...	...	$5.03^{+0.82}_{-0.97}$	$12.19^{+5.2}_{-2.73}$	16.1/18	$1.77^{+0.31}_{-0.41}$	$6.44^{+0.76}_{-0.63}$	16.91/18	$1.15^{+0.22}_{-0.2}$	$0.53^{+0.13}_{-0.11}$	BB+BB
10	2020-04-28T11:12:58.520	$1.82^{+0.09}_{-0.09}$	...	12.86/19	...	...	...	...	...	...	$1.38^{+0.15}_{-0.13}$	...	PL
11	2020-04-28T11:24:28.120	$1.72^{+0.21}_{-0.24}$	...	6.5/5	$6.97^{+1.39}_{-1.02}$	...	6.47/5	...	...	...	$0.6^{+0.16}_{-0.15}$	...	BB
12	2020-04-28T11:30:36.180	...	...	...	$11.21^{+1.7}_{-1.46}$	...	14.86/21	...	...	...	$0.67^{+0.12}_{-0.11}$	...	BB
13	2020-04-28T14:20:52.519	...	...	...	$1.36^{+0.1}_{-0.09}$	$4.66^{+0.4}_{-0.33}$	90.28/68	$2.29^{+0.08}_{-0.08}$	$1.89^{+0.12}_{-0.11}$	83.59/68	$0.44^{+0.04}_{-0.05}$	$0.48^{+0.05}_{-0.05}$	BB+PL
14	2020-04-28T14:20:57.900	$0.98^{+0.15}_{-0.17}$	$50.32^{+6.82}_{-5.11}$	54.98/50	$3.09^{+0.55}_{-0.47}$	$15.29^{+1.12}_{-0.94}$	50.83/49	...	...	...	$0.71^{+0.12}_{-0.11}$	$1.33^{+0.09}_{-0.09}$	BB+BB
15 <sup>g</sup>	2020-04-28T14:34:24.000	$1.56^{+0.06}_{-0.06}$	$37.00^{+3.99}_{-3.32}$	-	$1.63^{+0.04}_{-0.04}$	$14.46^{+0.25}_{-0.24}$	-	$1.93^{+0.04}_{-0.04}$	$11.32^{+0.55}_{-0.56}$	...	$5.95^{+0.34}_{-0.32}$	...	CPL
16	2020-04-28T17:15:26.237	$1.22^{+0.2}_{-0.21}$	$48.01^{+13.39}_{-7.8}$	32.54/19	$3.58^{+0.5}_{-0.53}$	$16.54^{+1.98}_{-1.6}$	29.43/18	$1.59^{+0.12}_{-0.13}$	$4.97^{+2.12}_{-0.99}$	35.58/18	$0.52^{+0.1}_{-0.09}$	$0.58^{+0.05}_{-0.06}$	BB+BB
17	2020-04-28T19:00:29.948	$1.65^{+0.19}_{-0.22}$	...	4.57/5	...	...	...	...	...	...	$0.64^{+0.13}_{-0.11}$	...	PL
18	2020-04-28T19:01:59.850	$0.94^{+0.12}_{-0.12}$	$33.78^{+2.17}_{-1.95}$	34.65/35	$2.2^{+0.21}_{-0.19}$	$11.63^{+0.47}_{-0.45}$	31.18/34	$2.16^{+0.13}_{-0.1}$	$10.7^{+0.61}_{-0.61}$	36.74/34	$4.53^{+0.2}_{-0.19}$	...	CPL
19	2020-04-29T00:17:40.942	...	...	...	$12.85^{+1.74}_{-1.46}$	...	14.58/15	...	...	...	$0.9^{+0.14}_{-0.12}$	...	BB
20	2020-04-29T11:12:39.397	$1.96^{+0.2}_{-0.2}$	...	28.11/13	$10.59^{+1.37}_{-1.2}$	...	26.77/13	...	...	...	$0.51^{+0.07}_{-0.07}$	...	BB
21	2020-04-29T11:13:57.650	$0.52^{+0.1}_{-0.1}$	$34.83^{+1.4}_{-1.29}$	73.7/76	$2.17^{+0.21}_{-0.2}$	$10.54^{+0.33}_{-0.32}$	69.52/75	$1.96^{+0.1}_{-0.09}$	$9.63^{+0.39}_{-0.39}$	73.25/75	$0.65^{+0.02}_{-0.02}$	...	CPL
22	2020-04-30T09:25:22.750	...	...	...	$13.01^{+2.12}_{-1.78}$	...	23.38/19	...	...	...	$0.26^{+0.05}_{-0.04}$	...	BB
23	2020-04-30T15:41:53.947	$1.53^{+0.17}_{-0.17}$	...	15.08/16	$15.66^{+2.29}_{-1.92}$	...	21.3/16	...	...	...	$0.72^{+0.11}_{-0.1}$	...	PL
24	2020-04-30T17:12:52.837	$1.22^{+0.11}_{-0.11}$	$24.74^{+1.72}_{-1.57}$	38.68/42	$2.36^{+0.17}_{-0.15}$	$10.97^{+0.57}_{-0.54}$	41.85/41	...	...	...	$1.84^{+0.09}_{-0.08}$	...	CPL
25	2020-05-01T15:05:56.635	$1.86^{+0.09}_{-0.08}$	...	29.07/31	...	...	...	...	...	...	$2.53^{+0.23}_{-0.2}$	...	PL
26	2020-05-01T15:15:20.876	$1.9^{+0.13}_{-0.13}$	...	28.66/16	$8.62^{+0.82}_{-0.74}$	...	23.34/16	...	...	...	$1.32^{+0.16}_{-0.16}$	...	BB
27	2020-05-02T05:40:53.151	$1.85^{+0.14}_{-0.15}$	...	6.79/9	...	...	...	...	...	...	$1.34^{+0.25}_{-0.22}$	...	PL
28	2020-05-02T10:17:26.000	$1.52^{+0.17}_{-0.19}$	$40.07^{+12.65}_{-7.4}$	28.68/36	$4.31^{+0.33}_{-0.33}$	$21.39^{+3.49}_{-2.82}$	29.2/35	$1.72^{+0.12}_{-0.15}$	$4.88^{+0.76}_{-0.58}$	22.31/35	$1.4^{+0.37}_{-0.37}$	$3.94^{+0.51}_{-0.47}$	BB+PL
29	2020-05-02T10:25:25.777	...	...	...	$1.54^{+0.17}_{-0.17}$	$15.5^{+1.2}_{-1.09}$	70.25/66	$1.82^{+0.16}_{-0.12}$	$15.74^{+4.08}_{-4.46}$	68.41/66	$0.09^{+0.03}_{-0.03}$	$0.46^{+0.06}_{-0.05}$	BB+PL
30	2020-05-02T10:46:20.850	$1.35^{+0.18}_{-0.19}$	...	8.01/9	...	...	...	...	...	...	$0.73^{+0.11}_{-0.1}$	...	PL
31	2020-05-03T04:30:59.050	...	...	...	$12.53^{+1.75}_{-1.51}$	...	29.81/16	...	...	...	$0.61^{+0.09}_{-0.08}$	...	BB
32	2020-05-03T17:12:55.600	$1.65^{+0.22}_{-0.23}$	...	21.57/27	...	...	...	...	...	...	$0.63^{+0.08}_{-0.09}$	...	PL
33 <sup>i</sup>	2020-05-03T23:25:13.250	$0.70^{+0.11}_{-0.10}$	$30.49^{+1.08}_{-1.14}$	306.84/281	$4.98^{+0.17}_{-0.16}$	$13.27^{+0.42}_{-0.39}$	308.77/280	...	...	...	$5.09^{+0.07}_{-0.06}$	...	CPL
34	2020-05-04T00:48:07.343	$1.73^{+0.06}_{-0.06}$	...	49.25/42	...	...	...	...	...	...	$0.98^{+0.06}_{-0.06}$	...	PL
35	2020-05-04T13:20:00.700	$1.37^{+0.16}_{-0.18}$	...	13.69/11	$17.93^{+2.66}_{-2.18}$	...	18.29/11	...	...	...	$0.66^{+0.08}_{-0.09}$	...	PL
36	2020-05-05T02:30:28.450	...	...	...	$15.23^{+3.11}_{-2.45}$	...	16.35/24	...	...	...	$0.31^{+0.06}_{-0.06}$	...	BB
37	2020-05-05T12:09:29.750	$1.82^{+0.14}_{-0.15}$	...	22.72/37	...	...	...	...	...	...	$3.01^{+0.28}_{-0.26}$	...	PL
38	2020-05-06T21:25:16.350	...	...	...	$10.17^{+0.7}_{-0.66}$	...	84.25/68	...	...	...	$0.33^{+0.03}_{-0.03}$	...	BB
39	2020-05-06T22:48:21.550	$1.63^{+0.24}_{-0.26}$	...	4.5/4	...	...	...	...	...	...	$0.76^{+0.15}_{-0.14}$	...	PL
40	2020-05-07T21:05:41.345	$1.47^{+0.17}_{-0.18}$	$31.15^{+6.38}_{-4.94}$	37.78/31	$2.38^{+0.25}_{-0.24}$	$13.51^{+1.14}_{-1.01}$	26.69/30	...	...	...	$1.38^{+0.22}_{-0.2}$	$1.39^{+0.13}_{-0.12}$	BB+BB
41	2020-05-08T06:17:16.589	$1.3^{+0.1}_{-0.1}$	$33.24^{+2.75}_{-2.38}$	58.77/46	...	...	...	$1.83^{+0.06}_{-0.06}$	$6.02^{+0.7}_{-0.58}$	64.73/45	$3.34^{+0.14}_{-0.13}$	...	CPL
42	2020-05-08T09:17:05.185	$1.82^{+0.15}_{-0.16}$	...	20.41/15	...	...	...	...	...	...	$2.17^{+0.3}_{-0.27}$	...	PL
43	2020-05-08T09:49:21.134	$1.21^{+0.22}_{-0.23}$	$46.68^{+15.31}_{-8.29}$	25.29/23	...	...	...	$1.82^{+0.25}_{-0.18}$	$11.22^{+3.27}_{-3.8}$	26.22/22	$1.21^{+0.11}_{-0.11}$	...	CPL
44	2020-05-08T19:23:36.028	$1.81^{+0.12}_{-0.13}$	...	18.34/13	...	...	...	...	...	...	$1.21^{+0.16}_{-0.15}$	...	PL
45	2020-05-08T19:37:25.270	$2.04^{+0.26}_{-0.26}$	...	12.69/16	...	...	...	...	...	...	$2.13^{+0.34}_{-0.31}$	...	PL
46	2020-05-09T01:56:38.750	...	...	...	$14.78^{+1.3}_{-1.16}$	...	28.52/32	...	...	...	$0.65^{+0.06}_{-0.06}$	...	BB
47	2020-05-10T05:00:28.195	$2.27^{+0.09}_{-0.08}$	...	100.96/80	$8.39^{+0.42}_{-0.4}$	...	100.41/80	...	...	...	$0.58^{+0.03}_{-0.03}$	...	BB
48 <sup>j</sup>	2020-05-10T06:12:01.622	$0.07^{+0.06}_{-0.06}$	$45.88^{+0.53}_{-0.53}$	410.74/378	...	...	...	...	...	...	$42.03^{+0.31}_{-0.31}$	...	CPL

**Table 4**  
(Continued)

Burst Information		CPL or PL			BB+BB or BB			BB+PL			Two Components		Selected Model <sup>e</sup>
ID	Trigger Time (UTC)	$\Gamma$	$E_{\text{peak}}$ (keV)	C-Stat/dof <sup>a</sup>	$kT_{\text{low}}$ (keV)	$kT_{\text{high}}$ (keV)	C-Stat/dof <sup>b</sup>	$\Gamma$	$kT$ (keV)	C-Stat/dof <sup>c</sup>	$\text{Flux}_1^d$	$\text{Flux}_2^d$	
49	2020-05-10T06:16:41.100	$1.16^{+0.15}_{-0.15}$	$44.68^{+8.17}_{-5.6}$	32.35/42	$2.56^{+0.28}_{-0.24}$	$14.13^{+1.0}_{-0.92}$	30.1/41	$1.82^{+0.13}_{-0.11}$	$11.93^{+1.92}_{-2.19}$	37.98/41	$0.41^{+0.02}_{-0.03}$	...	CPL
50	2020-05-10T06:20:09.400	$1.31^{+0.17}_{-0.18}$	$37.01^{+7.06}_{-4.89}$	27.9/23	...	...	...	$1.89^{+0.13}_{-0.11}$	$8.76^{+2.03}_{-1.75}$	28.23/22	$1.2^{+0.08}_{-0.08}$	...	CPL
51	2020-05-10T08:55:46.300	$1.17^{+0.12}_{-0.13}$	$38.29^{+4.39}_{-3.47}$	27.44/30	$2.32^{+0.23}_{-0.2}$	$12.92^{+0.7}_{-0.66}$	31.97/29	...	...	...	$1.5^{+0.08}_{-0.08}$	...	CPL
52	2020-05-10T18:53:01.040	...	...	...	$2.53^{+0.63}_{-0.59}$	$9.92^{+0.82}_{-0.74}$	79.92/65	$1.82^{+0.29}_{-0.19}$	$8.87^{+0.73}_{-0.71}$	84.35/65	$0.03^{+0.01}_{-0.0}$	$0.12^{+0.01}_{-0.01}$	BB+BB
53	2020-05-10T20:16:22.000	...	...	...	$2.74^{+0.63}_{-0.5}$	$10.56^{+1.13}_{-1.01}$	72.28/50	$1.72^{+0.29}_{-0.21}$	$8.84^{+1.11}_{-0.99}$	74.59/50	$0.05^{+0.01}_{-0.02}$	$0.15^{+0.01}_{-0.02}$	BB+BB
54 <sup>k</sup>	2020-05-10T21:51:16.221	$-0.08^{+0.05}_{-0.05}$	$33.64^{+0.40}_{-0.39}$	532.96/529	...	...	...	...	...	...	$22.22^{+0.18}_{-0.18}$	...	CPL
55	2020-05-10T22:08:09.000	$1.7^{+0.17}_{-0.17}$	...	8.84/12	...	...	...	...	...	...	$2.79^{+0.37}_{-0.35}$	...	PL
56	2020-05-11T04:22:52.560	$0.59^{+0.31}_{-0.34}$	$16.32^{+1.15}_{-1.2}$	16.08/16	$2.77^{+0.44}_{-0.38}$	$7.36^{+1.19}_{-0.94}$	16.59/15	$2.35^{+0.18}_{-0.18}$	$4.65^{+0.38}_{-0.33}$	16.7/15	$2.29^{+0.18}_{-0.17}$	...	CPL
57	2020-05-11T17:15:43.320	...	...	...	$3.42^{+0.29}_{-0.29}$	$13.64^{+1.54}_{-1.3}$	27.12/31	...	...	...	$0.89^{+0.09}_{-0.08}$	$0.52^{+0.05}_{-0.04}$	BB+BB
58	2020-05-12T08:35:19.700	$0.53^{+0.23}_{-0.26}$	$29.77^{+2.46}_{-2.19}$	17.72/17	$2.8^{+1.06}_{-0.54}$	$9.97^{+1.16}_{-0.71}$	20.27/16	$1.98^{+0.19}_{-0.17}$	$7.96^{+0.87}_{-0.81}$	22.45/16	$1.57^{+0.11}_{-0.1}$	...	CPL
59	2020-05-12T21:47:43.340	$1.29^{+0.25}_{-0.25}$	...	18.97/15	$20.46^{+4.88}_{-3.57}$	...	23.84/15	...	...	...	$1.00^{+0.22}_{-0.19}$	...	PL
60	2020-05-13T07:12:57.543	$0.92^{+0.28}_{-0.31}$	$14.7^{+1.43}_{-1.53}$	32.84/36	...	...	...	...	...	...	$1.02^{+0.1}_{-0.1}$	...	CPL
61	2020-05-14T14:49:22.000	$0.63^{+0.07}_{-0.08}$	$33.46^{+1.05}_{-1.0}$	88.06/80	...	...	...	...	...	...	$1.77^{+0.05}_{-0.04}$	...	CPL
62	2020-05-16T01:50:23.542	$1.19^{+0.13}_{-0.14}$	$36.1^{+4.36}_{-3.42}$	37.45/34	...	...	...	...	...	...	$1.66^{+0.09}_{-0.09}$	...	CPL
63	2020-05-16T10:26:32.309	$1.61^{+0.14}_{-0.16}$	...	12.81/19	...	...	...	...	...	...	$2.16^{+0.28}_{-0.26}$	...	PL
64	2020-05-16T11:16:17.000	$0.99^{+0.12}_{-0.13}$	$40.57^{+3.33}_{-2.85}$	37.06/39	$3.43^{+0.32}_{-0.3}$	$14.46^{+0.89}_{-0.78}$	32.72/38	...	...	...	$0.78^{+0.08}_{-0.09}$	$0.94^{+0.06}_{-0.05}$	BB+BB
65	2020-05-16T18:12:52.080	$1.27^{+0.08}_{-0.08}$	$35.47^{+2.39}_{-2.1}$	63.17/64	...	...	...	...	...	...	$4.05^{+0.14}_{-0.13}$	...	CPL
66	2020-05-17T03:18:10.320	$1.95^{+0.16}_{-0.17}$	...	22.03/19	...	...	...	...	...	...	$2.1^{+0.26}_{-0.23}$	...	PL
67	2020-05-18T01:54:21.550	...	...	...	$17.8^{+3.12}_{-2.51}$	...	188/23	...	...	...	$0.38^{+0.07}_{-0.06}$	...	BB
68	2020-05-18T05:17:57.715	$1.86^{+0.11}_{-0.11}$	...	17.62/14	...	...	...	...	...	...	$1.99^{+0.27}_{-0.25}$	...	PL
69	2020-05-18T09:27:59.151	$1.22^{+0.26}_{-0.31}$	...	4.88/11	...	...	...	...	...	...	$0.3^{+0.06}_{-0.05}$	...	PL
70	2020-05-18T11:00:41.150	...	...	...	$12.96^{+2.95}_{-2.24}$	...	14.56/12	...	...	...	$0.8^{+0.17}_{-0.16}$	...	BB
71	2020-05-18T16:28:18.300	...	...	...	$3.92^{+0.59}_{-0.57}$	$20.71^{+5.44}_{-3.73}$	47.85/28	$1.39^{+0.26}_{-0.36}$	$4.08^{+1.67}_{-0.89}$	485/28	$0.35^{+0.1}_{-0.09}$	$0.31^{+0.06}_{-0.05}$	BB+BB
72	2020-05-19T18:57:36.300	$0.93^{+0.15}_{-0.16}$	$35.1^{+2.68}_{-2.38}$	31.64/29	$2.82^{+0.31}_{-0.27}$	$12.33^{+0.63}_{-0.58}$	28.9/28	...	...	...	$6.08^{+0.31}_{-0.29}$	...	CPL
73	2020-05-20T14:10:49.780	$1.04^{+0.07}_{-0.08}$	$36.32^{+1.76}_{-1.59}$	76.14/71	...	...	...	...	...	...	$4.19^{+0.13}_{-0.12}$	...	CPL
74 <sup>l</sup>	2020-05-20T21:47:07.480	$0.69^{+0.04}_{-0.03}$	$34.17^{+0.74}_{-0.73}$	466.60.1/314	...	...	...	...	...	...	$6.02^{+0.07}_{-0.07}$	...	CPL
75	2020-05-24T22:05:03.480	...	...	...	$5.07^{+2.03}_{-2.44}$	$13.1^{+3.59}_{-2.12}$	18/24	...	...	...	$0.34^{+0.13}_{-0.13}$	$0.54^{+0.1}_{-0.09}$	BB+BB

**Notes.**

<sup>a</sup> C-Stat for the CPL model fit or PL fit.

<sup>b</sup> C-Stat for the BB+BB model fit or BB fit.

<sup>c</sup> C-Stat for the BB+PL model fit.

<sup>d</sup> Flux in 1–250 keV of different components of complex models ( $10^{-7}$  erg cm $^{-2}$  s $^{-1}$ ).

<sup>e</sup> The model we selected was used to calculate flux. A, B, C, D, and E represent CPL, BB+BB, BB+PL, PL, and BB models, respectively.

<sup>f</sup> Burst for which the HE data suffered from saturation with a constant of  $\text{factor}_{\text{HE}} = 0.39^{+0.04}_{-0.05}$ .

<sup>g</sup> The parameters of the FRB 200428-Associated Burst are from Li et al. (2021). CPL:  $\text{factor}_{\text{ME}} = 0.98^{+0.07}_{-0.06}$ ,  $\text{factor}_{\text{HE}} = 0.68^{+0.07}_{-0.07}$ ; BB+PL:  $\text{factor}_{\text{ME}} = 1.05^{+0.08}_{-0.07}$ ,  $\text{factor}_{\text{HE}} = 0.54^{+0.07}_{-0.06}$ .

<sup>h</sup> Burst for which the LE and HE data suffered from saturation with constants of  $\text{factor}_{\text{LE}} = 0.72^{+0.05}_{-0.05}$  and  $\text{factor}_{\text{HE}} = 0.64^{+0.04}_{-0.04}$ .

<sup>i</sup> Burst for which the HE data suffered from saturation with a constant of  $\text{factor}_{\text{HE}} = 0.44^{+0.02}_{-0.03}$  for the CPL model (BB+BB:  $\text{factor}_{\text{HE}} = 0.51^{+0.03}_{-0.04}$ ).

<sup>j</sup> Burst for which the HE data suffered from saturation with a constant of  $\text{factor}_{\text{HE}} = 0.15^{+0.01}_{-0.01}$ .

<sup>k</sup> Burst for which the LE and HE data suffered from saturation with constants of  $\text{factor}_{\text{LE}} = 1.05^{+0.06}_{-0.05}$  and  $\text{factor}_{\text{HE}} = 0.26^{+0.01}_{-0.01}$ .

<sup>l</sup> Burst for which the HE data suffered from saturation with a constant of  $\text{factor}_{\text{HE}} = 0.57^{+0.03}_{-0.02}$ .

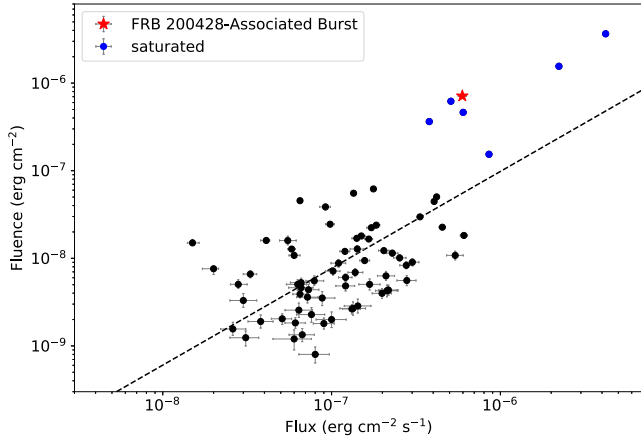


**Figure 10.** The scatter plot of the fluence vs. flux in 1–250 keV of each burst. The red star and blue circles represent the FRB 200428-Associated Burst and saturated bursts, respectively. There is a strong correlation between these two parameters. The black dashed line is the PL fit with an index of  $1.11 \pm 0.13$ .

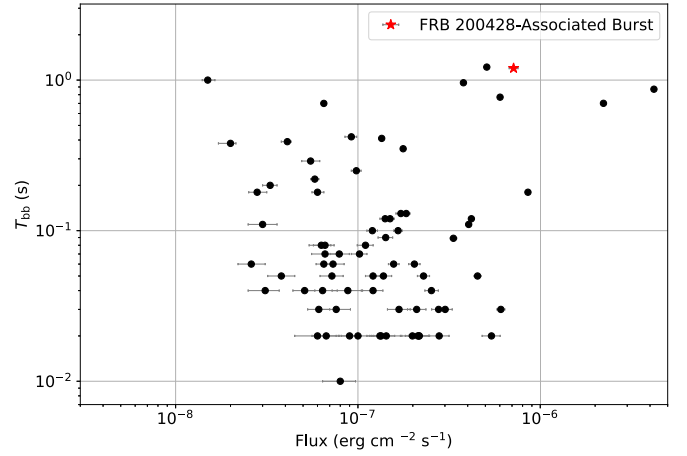
### 5.2. Burst Energies

For the 75 bursts from SGR J1935+2154 detected by Insight-HXMT, we find that the fluence is correlated with flux (both in the 1–250 keV range), as shown in Figure 10. To quantify this correlation, we compute the Spearman’s rank order correlation coefficient,  $\rho = 0.57$ , and the chance from a random data set,  $P = 4.86 \times 10^{-8}$ . A power law fitted to the mean values of the data using the least-squares technique yields an index of  $1.11 \pm 0.13$ . This correlation is not a surprise because the fluence is derived from the (averaged) flux and burst duration, and the distribution of duration is relatively narrow. Thus, we check the relation between averaged flux and duration, but we do not find a correlation between them (see Figure 11).

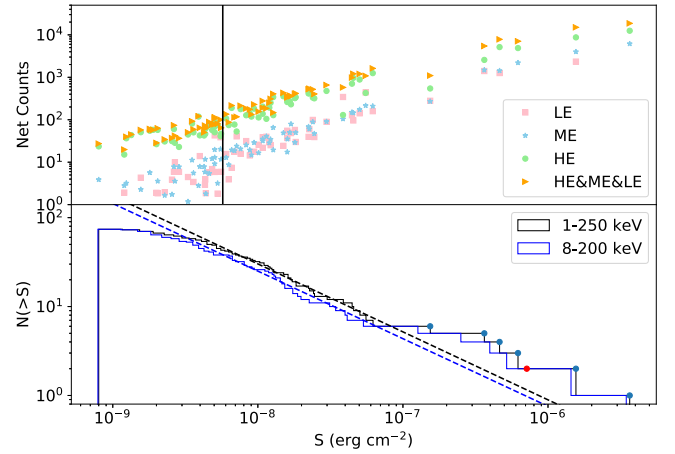
The cumulative distribution of the fluence ( $S$ ) of all 75 bursts is shown in the bottom panel of Figure 12. Since there are observational selection effects in the low-fluence region (less than about  $5 \times 10^{-9}$  erg cm $^{-2}$ ) and statistical fluctuation due to small numbers in the high-fluence end (greater than about  $1 \times 10^{-7}$  erg cm $^{-2}$ ), we focus on the distribution of those bursts between  $5 \times 10^{-9}$  erg cm $^{-2}$  and  $1 \times 10^{-7}$  erg cm $^{-2}$  (in 1–250 keV), which is well fit by a power law with a best-fit index of  $0.764 \pm 0.004$ . For a direct comparison with Fermi/GBM (8–200 keV) results (Lin et al. 2020b), we also fit the fluence in 8–200 keV of Insight-HXMT and get a best-fit PL index of  $0.760 \pm 0.007$ , which is basically the same as the result derived with fluence in 1–250 keV. This PL index is also comparable to the result reported for the previous active episodes from SGR J1935+2154 by Fermi/GBM (Lin et al. 2020a, 2020b) and other magnetars (Cheng et al. 1996; Collazzi et al. 2015). Younes et al. (2020) reported a PL fit with PL index of  $\sim 0.5$  to the fluence distribution of SGR J1935+2154 bursts during burst storms, but this measurement is done in a relatively narrower energy band (0.5–10 keV).

Thanks to its high sensitivity, Insight-HXMT unveiled many bursts with fluence less than  $1 \times 10^{-7}$  erg cm $^{-2}$ , below which the measurements of Fermi/GBM suffer observational effects and the burst energy distribution deviates from PL (Lin et al. 2020b). Thus, this Insight-HXMT measurement indicates that the bursts with lower fluence (less than  $1 \times 10^{-7}$  erg cm $^{-2}$ ) also follow the same PL distribution as that of higher-fluence bursts.

As mentioned before, there are apparent deviations seen in both the high- and low-fluence regions (bottom panel of



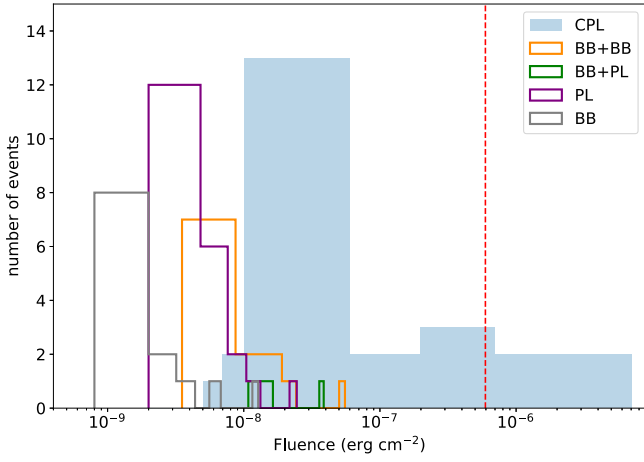
**Figure 11.** The scatter plot of  $T_{bb}$  and energy flux (1–250 keV). The red star is the FRB 200428-Associated Burst.



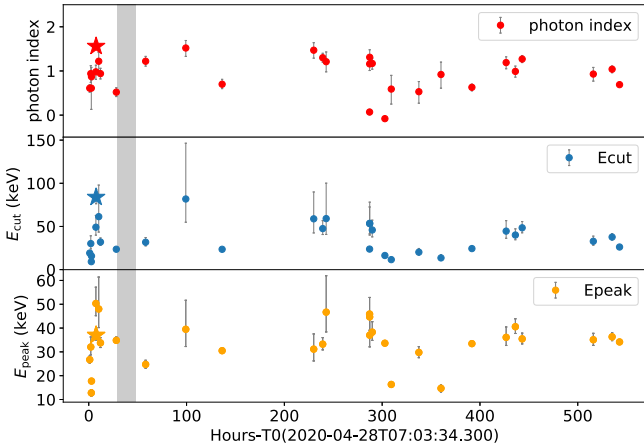
**Figure 12.** Top: the relation between the net counts and fluence. The orange triangles are the total net counts of HE, ME, and LE. The green circles, blue stars, and pink squares represent the net counts of HE, ME, and LE, respectively. The black solid line is the minimum fluence (1–250 keV) used for the PL fits. Bottom: the cumulative fluence distributions of SGR J1935+2154 bursts. The black and gray lines represent the energy ranges of 1–250 keV and 8–200 keV, respectively. The black and gray dashed lines are the best PL fit to the distribution of the range from  $5.73 \times 10^{-9}$  erg cm $^{-2}$  to  $1.09 \times 10^{-7}$  erg cm $^{-2}$  for 1–250 keV and from  $5.46 \times 10^{-9}$  erg cm $^{-2}$  to  $1.04 \times 10^{-7}$  erg cm $^{-2}$  for 8–200 keV, respectively. The indices of the PL fit are  $0.764 \pm 0.004$  for 1–250 keV and  $0.760 \pm 0.007$  for 8–200 keV. The blue and red circles represent the saturated bursts and the FRB 200428-Associated Burst, respectively.

Figure 12). For the high-fluence region (greater than about  $1 \times 10^{-7}$  erg cm $^{-2}$ ), which includes bright bursts (all are saturated), we calculate the expected cumulative event number by extrapolating the PL fit and find that these numbers in the seven bins are 6, 2, 2, 1, 1, 1, and 0, well consistent with the number of the detected events. Therefore, the deviation from the PL fit is very probably due to the statistical fluctuations of a small number of bursts.

As for the ramping feature in the low-fluence region, we caution that this deviation from the PL distribution could be easily misleading. It is the net counts (rather than the fluence) of each telescope that determine whether the burst could be triggered or not (see Paper I). We note that, since the fluence depends on the duration and spectral shape of a burst, bursts with basically the same net counts around the trigger threshold show a wide distribution of fluence extending below



**Figure 13.** The distribution of the fluence in 1–250 keV for each model. The blue, orange, green, purple, and gray lines represent CPL, BB+BB, BB+PL, PL, and BB models, respectively, for which the bursts are fit with the minimum BIC value. The red line is the FRB 200428-Associated Burst.



**Figure 14.** The evolution of the parameters of the CPL model. Photon index,  $E_{\text{cut}}$ , and  $E_{\text{peak}}$  are marked as red, blue, and orange circles, respectively. The stars represent the FRB 200428-Associated Burst. The gray shadow is the time interval of the incomplete monitoring of SGR J1935+2154.

$\sim 5 \times 10^{-9}$  erg cm $^{-2}$  (see the top panel of Figure 12). In principle, the detection efficiency of weak bursts is heavily affected by the instrumental sensitivity, search algorithm, and burst properties (e.g., duration, spectra). Therefore, the deviation of PL in the low-fluence end is caused by those factors.

Bursts could be grouped according to the good-fit spectral model (see Table 4), i.e., the model that gives the minimum BIC. We investigate the fluence distribution for bursts in each model group, as shown in Figure 13. We find that the high-fluence bursts are almost always fitted with the CPL model and weak bursts are always fitted with simple models (i.e., BB and PL). We note that it is possible that these weak bursts could also have complex spectral components (such as CPL, BB+BB, or PL+BB) but just have insufficient statistics to support the identification of complex models rather than simple ones.

### 5.3. Burst Evolution

To investigate how the spectral properties of bursts evolve throughout this burst episode of SGR J1935+2154, we plot the burst photon index, peak energies, and cutoff energies of bursts

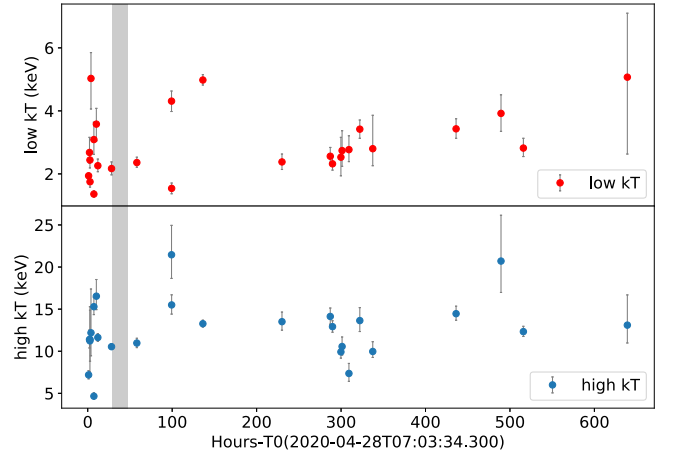


**Figure 15.** The evolution of the parameters of the BB+BB model. Low  $kT$  and high  $kT$  are marked as red and blue circles, respectively. The gray shadow is the time gap of the monitoring of SGR J1935+2154.

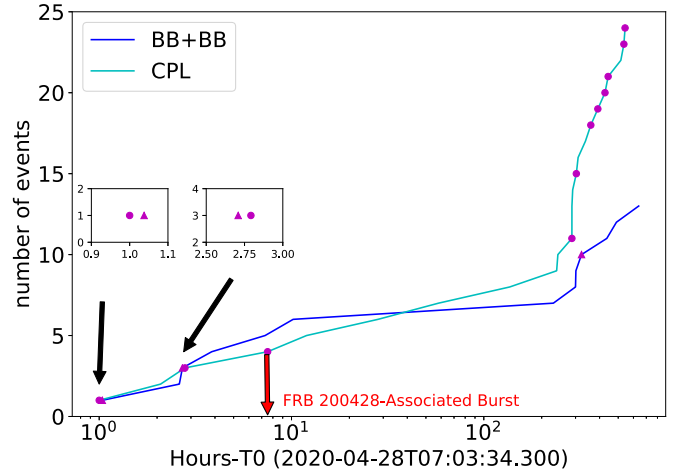


**Figure 16.** The evolution of the fitting models for CPL and BB+BB. The blue and green lines mark BB+BB models (13) and CPL models (24), respectively, for which the bursts are fit with the minimum BIC value. The triangles and circles that represent the preferred models are BB+BB models (3) and CPL models (11) using a BIC of  $\Delta > 10$  (see Section 3.2).

derived with the CPL models in Figure 14 and find that there is no significant evolution of these parameters. The high  $kT$  and low  $kT$  of the BB+BB model across this episode also have no significant evolution (Figure 15).

We present the temporal evolution of the preferred spectrum model (BB+BB or CPL) of the bursts in our sample in Figure 16. Interestingly, those bursts with CPL as the preferred model mostly occurred in the later part of this burst episode, where the burst rate is significantly lower than the active period (see Figure 5 in Paper I). We also check the fluence and flux of bursts (Figure 17) and find that there is no apparent evolution in the flux and fluence over time. We note that the FRB 200428-Associated Burst has high (but not the highest) flux and fluence with the preferred CPL spectral model and occurred in the early stage, where the burst rate is very high.

### 5.4. Burst Association with Radio Burst

In this burst sample of Insight-HXMT, there is only one burst associated with a radio burst, i.e., the FRB200428-Associated Burst, which has a longer duration (1.2 s; Li et al. 2021) than



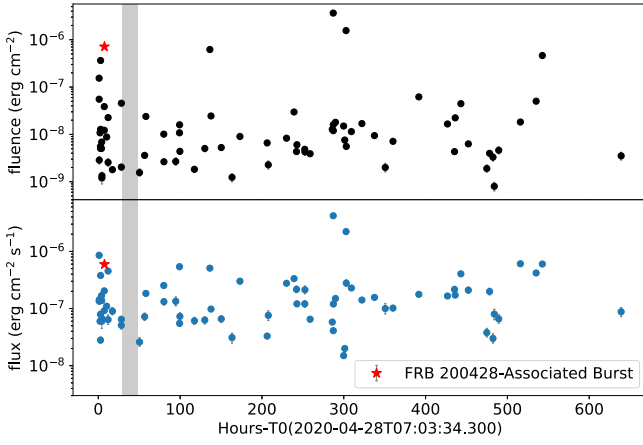


**Figure 17.** The evolution of fluence (top panel) and flux (bottom panel) in 1–250 keV. The stars represent the FRB 200428-Associated Burst. The gray shadow is the time gap of the monitoring of SGR J1935+2154 of Insight-HXMT.

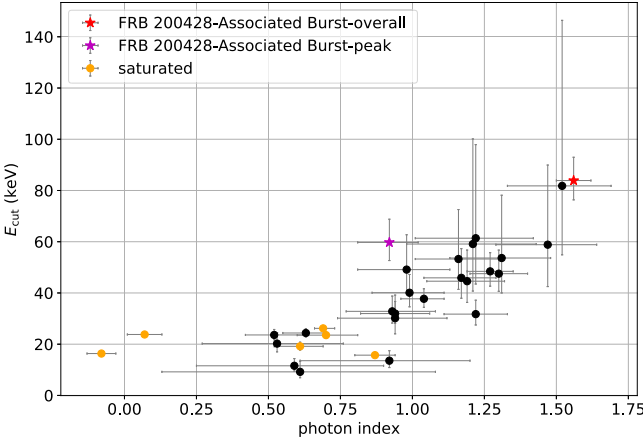


**Figure 18.** The scatter plot of  $E_{\text{cut}}$  and photon index. Orange circles represent the saturated bursts. The red and purple stars are the time-integral and peak spectra of FRB 200428-Associated Burst, respectively.

other bursts in the sample. If we consider the full period of the FRB 200428-Associated Burst (1.2 s), its  $E_{\text{peak}}$  ( $\sim 37$  keV) is not special (Figure 4), but the  $E_{\text{cut}}$  ( $\sim 84$  keV) and photon index ( $\sim 1.56$ ) are slightly higher than those of other bursts in our sample (right panels of Figures 2 and 5; see also Li et al. 2021).

Interestingly, there is one burst in our sample (burst #28) whose photon index ( $\sim 1.52$ ) and  $E_{\text{cut}}$  ( $\sim 82$  keV) resemble those of the time-integrated spectrum of the FRB 200428-Associated Burst, as shown in Figure 18. The light curve and spectrum of this burst are shown in Figures 19 and 20, respectively. This burst has a duration of about 0.02 s, which is much less than the full burst but comparable to the peak part of the FRB 200428-Associated Burst.

Li et al. (2021) identified that the FRB 200428-Associated Burst has two narrow peaks with a separation of  $\sim 30$  ms, consistent with the separation between the two bursts in FRB 200428. If we only consider the bright part of FRB200428-Associated Burst, which lasts for about 0.06 s, although both the photon index ( $\sim 0.9$ ) and  $E_{\text{cut}}$  ( $\sim 60$  keV) are not atypical (Figure 18), its  $E_{\text{peak}}$  ( $\sim 65$  keV) is somewhat high (which is also reported in Ridnaia et al. 2021). No other burst in this Insight-HXMT sample has such a high  $E_{\text{peak}}$  (Figure 4).

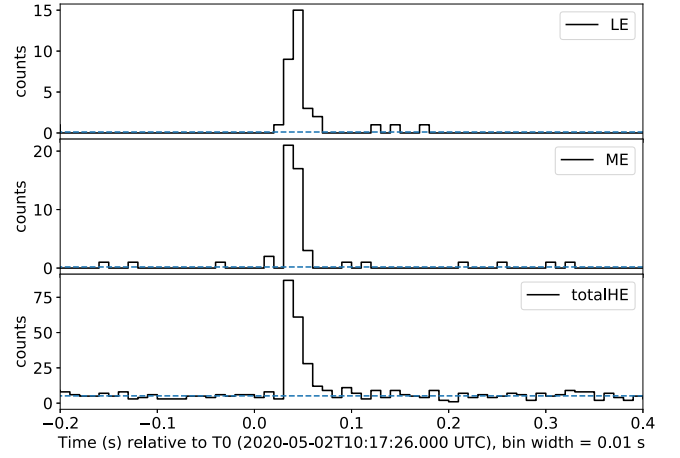


**Figure 19.** The light curves of the burst whose spectrum resembles that of the FRB 200428-Associated Burst. The light curves observed with LE (1–10 keV), ME (10–30 keV), and HE (28–250 keV) with a time resolution of 10 ms are shown in the top, middle, and bottom panels, respectively.

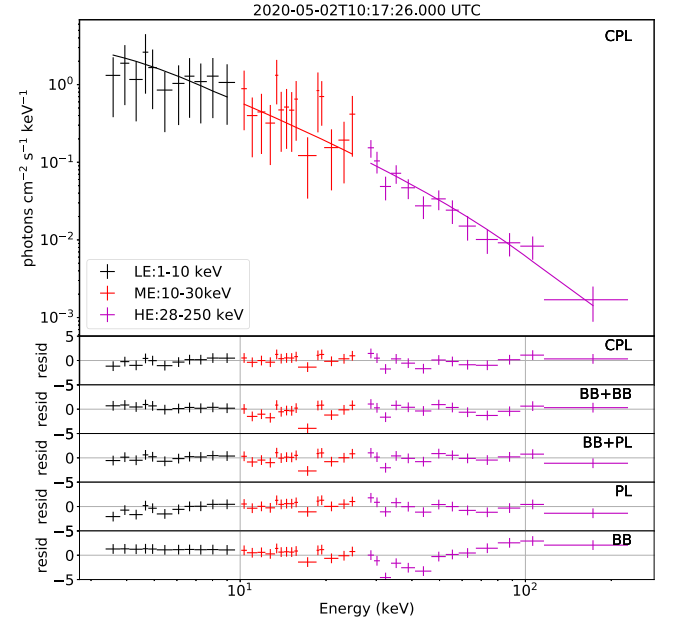


**Figure 20.** The spectrum of the SGR J1935+2154 burst whose spectrum resembles that of FRB 200428-Associated Burst. Data from LE, ME, and HE of Insight-HXMT are represented in different colors (LE: black; ME: red; HE: purple). The X-ray spectrum of the burst described by the CPL model is shown in the top panel. The five lower panels are the residuals of the data from the individual models of CPL, BB+BB, BB+PL, PL, and BB.

We checked the radio observational campaign of SGR J1935+2154 and found that there were radio observations (e.g., CHIME/Pulsar, Northern Cross radio telescope) of this source during this burst but without any detection of radio bursts from SGR 1935+2154 (Tan & Chime/Pulsar Collaboration 2020; Naldi et al. 2020).

## 6. Summary

In this paper, we report the detailed results of time-integrated spectral analyses of the 75 bursts from SGR J1935+2154 detected by Insight-HXMT during the dedicated 33 day ToO observation. The wide energy range (1–250 keV) and high sensitivity of Insight-HXMT allow for accurate spectral characterization of magnetar bursts.



Five spectral models are adopted to fit the spectra: the sum of two blackbody functions (BB+BB), cutoff power law (CPL), blackbody and power-law functions (BB+PL), power law (PL), and single blackbody (BB). The Insight-HXMT and Fermi/GBM joint fits show that the preferred model can be more easily identified when Insight-HXMT data in a broader energy band are used in the joint fitting. For  $\sim 15\%$  of the 75 bursts, the CPL model is preferred. The photon index and  $E_{\text{peak}}$  of CPL model for 30 bursts center at the mean value of 1.04 and 34.14 keV, respectively. The temperatures of low and high BB components of the BB+BB model center around  $\sim 2.9$  and  $\sim 12.1$  keV, respectively.

The burst fluences range from  $\sim 10^{-9}$  to  $\sim 10^{-6}$  erg cm $^{-2}$  in the energy range of 8–200 keV. Although these bursts detected by Insight-HXMT in this observation campaign are less energetic, the cumulative distribution of fluence follows the same power-law trend as that of brighter bursts reported by Fermi/GBM. We find that the deviation of the weaker bursts from the power law of the cumulative fluence distribution is due not only to the instrument sensitivity and burst search algorithm but also to the difference of the duration and spectral shape of bursts. We also find that the bursts with the preferred CPL model mostly occurred in the later epoch of this activity period.

An interesting single-pulse burst is found to be similar to the time-integrated spectrum of FRB 200428-Associated Burst. However, it is different from the spectrum of the peak of the FRB 200428-Associated Burst, which is directly related to the FRB. The time-resolved analysis of bursts is also crucial to study the detailed physics, and we leave it for future work.

We thank the anonymous reviewer for very helpful comments and suggestions. We are grateful to Prof. Shri Kulkarni for suggesting the 1 month observation after the initial ToO of SGR J1935+2154. This work is supported by the National Key R&D Program of China (2021YFA0718500). The authors acknowledge support from the Strategic Priority Research Program on Space Science, the Chinese Academy of Sciences (grant Nos. XDA15360300, XDA15052700, XDB23040400), and the National Natural Science Foundation of China (grant Nos. U1838201, U1838202, U1838113, U2038106, U1938201, 12133007, 11961141013).

#### ORCID iDs

Ce Cai  <https://orcid.org/0000-0002-6540-2372>  
Shao-Lin Xiong  <https://orcid.org/0000-0002-4771-7653>

Lin Lin  <https://orcid.org/0000-0002-0633-5325>  
Cheng-Kui Li  <https://orcid.org/0000-0001-5798-4491>  
Shuang-Nan Zhang  <https://orcid.org/0000-0001-5586-1017>  
You-Li Tuo  <https://orcid.org/0000-0003-3127-0110>  
Li-Ming Song  <https://orcid.org/0000-0003-0274-3396>  
Fang-Jun Lu  <https://orcid.org/0000-0003-3248-6087>

#### References

- Bochenek, C. D., Ravi, V., Belov, K. V., et al. 2020, *Natur*, **587**, 59  
Cai, C., Xue, W., Li, C., et al. 2022, *ApJS*, **260**, 24  
Cao, X., Jiang, W., Meng, B., et al. 2019, *SCPMA*, **63**, 249504  
Cash, W. 1979, *ApJ*, **228**, 939  
Chen, Y., Cui, W., Li, W., et al. 2019, *SCPMA*, **63**, 249505  
Cheng, B., Epstein, R. I., Guyer, R. A., & Young, A. C. 1996, *Natur*, **382**, 518  
CHIME/FRB Collaboration, Andersen, B. C., Bandura, K. M., et al. 2020, *Natur*, **587**, 54  
Collazzi, A. C., Kouveliotou, C., van der Horst, A. J., et al. 2015, *ApJS*, **218**, 11  
Hurley, K., Cline, T., Mazets, E., et al. 1999, *Natur*, **397**, 41  
Israel, G. L., Esposito, P., Rea, N., et al. 2016, *MNRAS*, **457**, 3448  
Israel, G. L., Romano, P., Mangano, V., et al. 2008, *ApJ*, **685**, 1114  
Kaneko, Y., Göğüş, E., Baring, M. G., et al. 2021, *ApJL*, **916**, L7  
Kouveliotou, C., Dieters, S., Strohmayer, T., et al. 1998, *Natur*, **393**, 235  
Li, C. K., Lin, L., Xiong, S. L., et al. 2021, *NatAs*, **5**, 378  
Li, X., Li, X., Tan, Y., et al. 2020, *JHEAp*, **27**, 64  
Lin, L., Göğüş, E., Baring, M. G., et al. 2012, *ApJ*, **756**, 54  
Lin, L., Göğüş, E., Roberts, O. J., et al. 2020a, *ApJ*, **893**, 156  
Lin, L., Göğüş, E., Roberts, O. J., et al. 2020b, *ApJL*, **902**, L43  
Lin, L., Kouveliotou, C., Baring, M. G., et al. 2011, *ApJ*, **739**, 87  
Lin, L., Zhang, C. F., Wang, P., et al. 2020c, *Natur*, **587**, 63  
Liu, C. Z., Zhang, Y. F., Li, X. F., et al. 2019, *SCPMA*, **63**, 249503  
Mazets, E. P., Golentskii, S. V., Ilinskii, V. N., Aptekar, R. L., & Guryan, I. A. 1979, *Natur*, **282**, 587  
Mereghetti, S., Savchenko, V., Ferrigno, C., et al. 2020, *ApJL*, **898**, L29  
Naldi, G., Pilia, M., Bernardi, G., et al. 2020, *ATel*, **13739**, 1  
Olausen, S. A., & Kaspi, V. M. 2014, *ApJS*, **212**, 6  
Palmer, D. M., Barthelmy, S., Gehrels, N., et al. 2005, *Natur*, **434**, 1107  
Ridnaia, A., Svinkin, D., Frederiks, D., et al. 2021, *NatAs*, **5**, 372  
Roberts, O. J., Veres, P., Baring, M. G., et al. 2021, *Natur*, **589**, 207  
Stamatikos, M., Malesani, D., Page, K. L., & Sakamoto, T. 2014, *GCN*, **16520**, 1  
Tan, C. M. & Chime/Pulsar Collaboration 2020, *ATel*, **13838**, 1  
Tavani, M., Casentini, C., Ursi, A., et al. 2021, *NatAs*, **5**, 401  
Thompson, C., & Duncan, R. C. 1995, *MNRAS*, **275**, 255  
Turolla, R., Zane, S., & Watts, A. L. 2015, *RPPH*, **78**, 116901  
van der Horst, A. J., Kouveliotou, C., Gorgone, N. M., et al. 2012, *ApJ*, **749**, 122  
Younes, G., Baring, M. G., Kouveliotou, C., et al. 2021, *NatAs*, **5**, 408  
Younes, G., Güver, T., Kouveliotou, C., et al. 2020, *ApJL*, **904**, L21  
Younes, G., Kouveliotou, C., Jaodand, A., et al. 2017, *ApJ*, **847**, 85  
Zhang, S., Zhang, S. N., Lu, F. J., et al. 2018, *Proc. SPIE*, **10699**, 106991U  
Zhang, S. N., Li, T. P., Lu, F. J., et al. 2019, *SCPMA*, **63**, 249502